Separation Flow Control with Vortex Generator Jets Employed in an Aft-Loaded Low-Pressure Turbine Cascade with Simulated Upstream Wakes

Thesis

Presented in Partial Fulfillment of the Requirements for the Degree Master of Science in the Graduate School of The Ohio State University

By

Kyle Adler Gompertz, B.S.

Graduate Program in Aerospace Engineering

The Ohio State University

2009

Thesis Committee:

Jeffrey P. Bons, Advisor

James W. Gregory

ABSTRACT

Detailed pressure and velocity measurements were acquired at Re_c = 20,000 with 3% inlet free stream turbulence intensity to study the effects of position, phase and forcing frequency of vortex generator jets employed on an aft-loaded low-pressure turbine blade in the presence of impinging wakes. The L1A blade has a design Zweifel coefficient of 1.34 and a suction peak at 58% axial chord, making it an aft-loaded pressure distribution. At this Reynolds number, the blade exhibits a non-reattaching separation region beginning at 60% axial chord under steady flow conditions without upstream wakes. Wakes shed by an upstream vane row are simulated with a moving row of cylindrical bars at a flow coefficient of 0.91. Impinging wakes thin the separation zone and delay separation by triggering transition in the separated shear layer, although the flow does not reattach. Instead, at sufficiently high forcing frequencies, a new time-mean separated shear layer position is established which begins at approximately 72%C_x. Reductions in area-averaged wake total pressure loss of more than 75% were documented. One objective of this study was to compare pulsed flow control using two rows of discrete vortex generator jets (VGJs). The VGJs are located at 59%C_x, approximately the peak C_p location, and at 72%C_x. Effective separation control was achieved at both locations. In both cases, wake total pressure loss decreased 35% from the wake only level and the shape of the C_p distribution indicates that the cascade recovers its high Reynolds number (attached flow) performance. The most effective separation control was achieved when actuating at 59%C_x where the VGJ disturbance dominates the dynamics of the separated shear layer, with the wake disturbance assuming a secondary role only. On the other

hand, when actuating at 72%C_x, the efficacy of VGJ actuation is derived from the relative mean shear layer position and jet penetration. When the pulsed jet actuation (25% duty cycle) was initiated at the 72%C_x location, synchronization with the wake passing frequency (8.7Hz) was critical to produce the most effective separation control. A 20% improvement in effectiveness over the wake-only level was obtained by aligning the jet actuation between wake events. A range of blowing ratios was investigated at both locations to maximize separation reduction with minimal mass flow. The optimal control parameter set for VGJ actuation at 72%C_x does not represent a reduction in required mass flow compared to the optimal parameter set for actuation at 59%C_x. Differences in the fundamental physics of the jet interaction with the separated shear layer are discussed and implications for the application of flow control in a full engine demonstrator are reviewed. Evidence suggests that flow control using VGJs will be effective in the highly unsteady LPT environment of an operating gas turbine, provided the VGJ location and amplitude are adapted for the specific blade profile.

DEDICATION

For my mother

ACKNOWLEDGEMENTS

It has been a tremendous privilege, learning from my advisor, Dr. Jeffrey Bons. I would like to express the utmost gratitude for his patience and support and inspiration.

I would like to thank my esteemed colleagues for their assistance during this endeavor. Specifically, I would like to thank Jon Pluim and Matthew Bloxham for generously sharing their time and knowledge.

I would like to acknowledge the support of the Air Force. Special thanks to Drs. Rolf Sondergaard and Richard Rivir, without whom I would have been at a loss for streamwise vorticity when I needed it most.

Thanks to my family members for their support, and to my mother I am most grateful.

VITA

January 18, 1984……. Born in Rapid City, South Dakota

2007…….B.S. Aerospace Engineering,
The Ohio State University

2007 – present……. Graduate Research Associate, Department
of Aerospace Engineering, The Ohio State University

Publications

1. Bons, J.P., Pluim, J., Gompertz, K., Bloxham, M., Clark, J.P., 2008, "The Application of Flow Control to an Aft-Loaded Low Pressure Turbine Cascade with Unsteady Wakes," presented at the 2008 IGTI conference in Berlin, June, 2008. Paper #GT2008-50864.
2. Gompertz, K., Pluim, J., Bons, J.P., 2009, "Separation Control Authority of Vortex Generating Jets in a Low-Pressure Turbine Cascade with Simulated Wakes," presented at the 2009 ASM conference in Orlando, 5-9 January, 2009. Paper #AIAA 2009-0377.

Fields of Study

Major Field: Aerospace Engineering

TABLE OF CONTENTS

Page

ABSTRACT ii

DEDICATION iv

ACKNOWLEDGEMENTS v

VITA vi

TABLE OF CONTENTS vii

LIST OF FIGURES ix

NOMENCLATURE xii

CHAPTER ONE: INTRODUCTION 1

1.1. Motivation 1

1.2. Flow Control: VGJs 2

1.3. The L1A LP Turbine Blade Profile 3

1.4. Simulating Periodically Impinging Wakes 4

1.5. Shear Layers and the Kelvin-Helmholtz Instability Mode 8

1.6. The Present Study 10

CHAPTER TWO: EXPERIMENTAL METHODS 12

2.1. Low-Speed Wind Tunnel 12

2.2. Test Section 12

2.2.1. L1A 12

2.2.2. Wake Generator 14

2.2.3. Vortex Generator Jets 16
2.3. Data Acquisition and Processing 18
2.3.1. Integrated Wake Loss (γ_{int}) 18
2.3.2. Hot-film Velocity Measurements 18
2.3.3. Particle Image Velocimetry 20
CHAPTER THREE: RESULTS AND DISCUSSION 22
3.1. Steady State L1A (No Wakes, No VGJs) 22
3.2. L1A with Unsteady Wakes + VGJs 29
3.2.1. C_p and γ_{int} Analysis of VGJ Synchronization and Chordwise Location 29
3.2.2. Hot-film Velocity Data Analysis for two Forcing Frequencies 32
3.2.3. γ_{int} Analysis of VGJ Blowing Ratio and Chordwise Location 46
3.2.4. Two-Dimensional Phase-Locked PIV Data 48
CHAPTER FOUR: CONCLUSION 68
BIBLIOGRAPHY 70
APPENDIX A: Intermittency Data 73
APPENDIX B: Instantaneous PIV images 76

LIST OF FIGURES

Figure 1: Schematic of L1A linear cascade. *Wake generator located 31%C_x upstream of cascade leading edge, wake total pressure surveys acquired 24%C_x downstream of cascade trailing edge plane.* 13

Figure 2: CAD model of wake generator and test section of tunnel. *Wake generator located 31%C_x upstream of cascade leading edge. Curved white arrows indicate direction of rotation. Straight arrow points to location of optical sensor.* 15

Figure 3: Pulsed VGJ blowing ratio plotted against dimensionless time. *VGJs at 59% and 72%C_x; indicating the implemented phase of VGJ actuation with respect to the wake sensor; t/T = 0 corresponds to signal from optical wake cylinder sensor; blue triangles indicate the center of 24 measurement phases for phase-locked data acquisition.* 17

Figure 4: The data collection region (left) and coordinate system used to present 2-D PIV data (right). *Left: the green plane represents the laser sheet, located 4d below the top of a midspan VGJ. Right: the dashed red line represents the PIV camera measurement window; the dashed green line indicates the cropped window for data presented herein; also included are the axial chord lines for the L1A.* 20

Figure 5: Predicted [22] and measured (Exp.) C_p values for immersed L1A blades at three Reynolds numbers. *The designation "inner" and "outer" is consistent with Fig. 1.* 23

Figure 6: Predicted [22] and measured area-averaged wake total pressure loss (γ_{int}) vs. Reynolds number for L1A. 25

Figure 7: Hot-film results for steady state boundary layer of the L1A at Re_c = 20,000. *Contour plots of u_{mean}/U_{in} (top), u_{rms}/U_{in} [%] (middle), and intermittency (bottom) presented in wall normal vs. axial chord coordinates.* 26

Figure 8: Suction surface acceleration parameter plotted against x/C_x. *Calculated from predicted and measured C_p data in Fig. 5 (*Re_c *= 60,000).* 28

Figure 9: Time-averaged shear layer comparison. *Data shown for steady state, wake-only (F_{red} = 0.41 & 0.20), and wake + VGJ actuation at 72%C_x (F_{red} = 0.41 & 0.20) cases. Upstream and downstream boundaries formed by constant curves of u_{rms}/U_{in} = 10% and 20% respectively. The*

solid or dashed line between boundaries formed by constant curves of u_{rms}/U_{in} = 15%. Re_c = *20,000.*..... 29

Figure 10: C_p data for steady state, wakes, wakes + upstream VGJ, and wakes + downstream VGJ cases at Re_c = 20,000 compared to prediction for L1A. 30

Figure 11: Wake total pressure loss normalized by loss with wakes only, plotted against dimensionless time. Data for VGJ actuation at 59% and 72%C_x. Re_c = *20,000,* F_{red} = *0.41,* B_{max} = *2. The abscissa is actuation time non-dimensionalized by the wake passing period, where* t/T = *0 is the time that each wake cylinder passes the optical sensor as it exits the cascade.* 31

Figure 12: Depiction of perturbation velocity field formulation. *Phase-locked* u_{mean}/U_{in} *data shown for phase 13 of 24 (top) minus the cycle average* u_{mean}/U_{in} *data (middle) yields the normalized perturbation velocity field of phase 13. The dashed green line on the* u_{mean} *plot at* y/C_x = *0.05 is the wall normal level shown in the time-space plots in later figures.* 33

Figure 13: Time-resolved contours of u_{rms}/U_{in} & $\Delta u_{mean}/U_{in}$ for wakes-only case with F_{red} = 0.41, Re_c =20,000. *Phases 1-12 of 24.*..... 35

Figure 14: Time-resolved contours of u_{rms}/U_{in} & $\Delta u_{mean}/U_{in}$ for wakes + DS VGJs with F_{red} = 0.41, Re_c =20,000. *Phases 1-12 of 24.*..... 37

Figure 15: Time-space plots at y/C_x = 0.049 of u_{mean}/U_{in}, u_{rms}/U_{in}, and intermittency for wakes only and wakes + VGJs at 72%C_x. F_{red} = *0.41,* Re_c = *20,000. Green highlighted band indicates separated shear layer location for steady state case.* 41

Figure 16: Time-space plots at y/C_x = 0.049 of u_{mean}/U_{in}, u_{rms}/U_{in}, and intermittency for wakes only and wakes + VGJs at 72%C_x (dropped rod). F_{red} = *0.20,* Re_c = *20,000. Green highlighted band indicates separated shear layer location for steady state case.* 42

Figure 17: Wake total pressure loss normalized by loss with wakes only plotted against blowing ratio. *Data for VGJ actuation at 59% and 72%*C_x *on the suction surface of the L1A, optimally synchronized with simulated unsteady wakes,* F_{red} = *0.41,* Re_c = *20,000.* 47

Figure 18: Sample figure from wakes-only case (F_{red} = 0.41), contours of fluctuating velocity magnitude superposed with perturbation velocity vectors. *Showing the existence of a vortical quadrupole structure whose saddle point is near the intersection of the black dashed lines. The naming convention is indicated by the symbols at the eye of each vortex.*..... 49

Figure 19: Ensemble-averaged streamwise velocity profiles for wakes-only (F_{red} = 0.41) at Re_c = 20,000. *Showing 8 of 24 measurement phases {phases 1,4,7,10,13,16,19,22}.* 55

Figure 20: Contours of fluctuating velocity magnitude (U_{rms}/U_{in}) superposed with perturbation velocity vectors ($\Delta U_{mean}/U_{in}$), data for wakes-only (F_{red} = 0.41) at Re_c = 20,000. *Showing 8 of 24 measurement phases {phases 1,4,7,10,13,16,19,22}.* 56

Figure 21: Contours of ensemble-averaged velocity magnitude (U_{mean}/U_{in}), data for wakes-only (F_{red} = 0.41) at Re_c = 20,000. *Showing 8 of 24 measurement phases.* 57

Figure 22: Contours of ensemble-averaged swirl strength (*Sw*), data for wakes-only (F_{red} = 0.41) at Re_c = 20,000. *Phases1 - 8.* 58

Figure 23: Ensemble-averaged streamwise velocity profiles for wakes + VGJs at 72%C_x (F_{red} = 0.41) at Re_c = 20,000. *Showing 8 of 24 measurement phases {1,4,7,10,13,16,19,22}.* 61

Figure 24: Contours of fluctuating velocity magnitude (U_{rms}/U_{in}) superposed with perturbation velocity vectors ($\Delta U_{mean}/U_{in}$), data for wakes + VGJs at 72%C_x (F_{red} = 0.41) at Re_c = 20,000. *Showing 8 of 24 measurement phases {phases 1,4,7,10,13,16,19,22}.* 62

Figure 25: Contours of ensemble-averaged velocity magnitude (U_{mean}/U_{in}), data for wakes + VGJs at 72%C_x (F_{red} = 0.41) at Re_c = 20,000. *Showing 8 of 24 measurement phases.* 63

Figure 26: Contours of ensemble-averaged swirl strength (*Sw*), data for wakes-only (F_{red} = 0.41) at Re_c = 20,000. *Showing 8 of 24 measurement phases {phases 1,4,7,10,13,16,19,22}.* 64

Figure 27: Contours of intermittency for wakes-only (F_{red} = 0.41), Re_c = 20,000. *Showing all 24 measurement phases.* 74

Figure 28: Contours of intermittency for wakes + VGJs at 72%C_x (F_{red} = 0.41), Re_c = 20,000. *Showing all 24 measurement phases.* 75

Figure 29: Collage of representative snapshots throughout the wake-passing period showing streamlines for wake-only case (F_{red} = 0.41), Re_c = 20,000. 78

NOMENCLATURE

B_{max}	blowing ratio ($U_{jet}/U_{e,\%Cx}$)
C_x	blade axial chord (0.143m)
C_p	pressure coefficient ($P_{T,in}$-P)/($P_{T,in}$-$P_{S,in}$)
c	blade true chord (0.156m)
D	wake generator cylinder diameter (4mm)
DS	refers to jets positioned at 72%C_x
d	jet hole diameter (2.6mm)
ê	unit vector
F^+	non-dimensional forcing frequency of VGJs (f/(U_{avg}/$SSLJ$))
F_{red}	wake reduced frequency [f/(U_{ex}/c)]
f	forcing frequency of VGJ actuation and wake passing (4.35 or 8.7Hz)
K	acceleration parameter (Eqn. 3)
L	wake generator cylinder spacing
P	pressure
Re_c	axial chord Reynolds number ($\rho U_{in} C_x/\mu$)
S	blade spacing
Sr	dimensionless Strouhal number
$SSLJ$	suction side length from jet location to trailing edge
Sw	swirl strength parameter
T	cylinder passing period (115 or 230ms)
t	time (s)
U	velocity magnitude
US	refers to jets located at 59%C_x
VGJ	vortex generator jet
u	streamwise velocity component
v	surface-normal velocity component
x	streamwise coordinate
y	blade normal coordinate
z	spanwise coordinate
Zw	Zweifel coefficient
γ_{int}	integrated wake total pressure loss coefficient (Eqn. 1)

Δu_{mean}	perturbation of mean velocity value from the cycle average
θ	momentum thickness
μ	dynamic viscosity
ν	kinematic viscosity
ρ	density
Φ	flow coefficient ($U_{in,axial}/U_{cyl}$)
ψ	blade loading parameter (Eqn. 2)

Subscripts

avg	average from jet location to trailing edge
axial	normal to cascade inlet plane
c	axial chord
con	refers to vortex convective velocity
cycleavg	average over cycle
cyl	refers to wake generator carbon fiber cylinder rod
e	local boundary layer edge
ex	refers to conditions at the cascade exit plane
in	refers to conditions at the cascade inlet plane
jet	VGJ conditions
max	maximum over a cycle
mean	mean
rms	root mean square
S	static
s	refers to conditions at separation location
T	total
$_{59\%Cx}$	*upstream* jet injection location
$_{72\%Cx}$	*downstream* jet injection location

CHAPTER ONE: INTRODUCTION

1.1. Motivation

With the trend toward higher bypass ratios in turbofans, demands are increasing for the low pressure turbines (LPT) that drive the large fan assemblies. Also, many military and civilian applications use the LPT to power an ever increasing array of onboard communication, diagnostic, and service hardware. At the same time, efforts are constantly underway to reduce engine weight and part count, particularly in the turbine which represents nearly 30% of the engine weight and 40% of the life cycle cost for parts replacement and servicing. With more work expected from a single turbine stage, the implication of turbine blade stall (or boundary layer separation) has even greater significance for overall engine performance. The strong adverse pressure gradient experienced on the suction side of turbine airfoils has been shown to result in significant aerodynamic losses, and a reduction in the work extracted from the through flow [1]. Also, pushing the turbine to the limits of its aerodynamic capabilities leaves little room for adapting to off-design conditions (e.g. from max thrust at take-off to high altitude cruise). Modern compressors make use of variable stators to successfully negotiate changes in operating conditions. Due to the elevated temperatures and rapidly expanding throughflow area in the turbine, adaptive structures have yet to be incorporated into the "hot section". However, several researchers have been exploring effective means of controlling LPT flow fields with aerodynamic flow control such as passive trips [2,3], plasma actuators [4], synthetic jets [5,6], and vortex

generating jets [7-15]. The on-demand, active control techniques have the advantage that they can be deactivated when not needed.

1.2. Flow Control: VGJs

Much of the research in LPT boundary layer separation has been conducted in low-speed linear cascades. A principal assumption in these studies is that the hub-to-tip ratio of the turbomachinery component in question is sufficiently close to unity that the annular configuration can be unwrapped and approximated as linear. Much of the focus concerning separation control has been with the Pack B blade (a highly loaded Pratt Whitney experimental profile) at low Reynolds number (Re based on axial chord and inlet velocity < 30,000). Considerable success has been achieved using VGJs with this blade profile in low-speed linear cascade facilities. Steady blowing VGJs have been shown to generate two counter-rotating streamwise vortices, of which one is dominant. The core of the coherent primary vortex promotes mixing as it convects downstream, entraining high momentum fluid in the free stream which energizes the boundary layer and suppresses the separated zone. Pulsed blowing has been shown to be at least as effective as analogous steady blowing using significantly less mass flow. This is attributed to the starting vortex ring at the onset of each pulse [7], which enables the vortex core to penetrate further into the boundary layer. A reduction in wake total pressure loss of up to 60% is typically reported. When the cascade studies add more realistic inlet conditions (3-5% inlet freestream turbulence [11,13] and/or unsteady wakes [14], the low Re separation is reduced and the gains from VGJs are more modest (20-30%). Still, there is a desire to explore flow control opportunities with more aggressive blade designs to discover what the limitations are. In this vein, Sondergaard et al. [16] reduced their cascade solidity (by increasing blade spacing at constant axial chord) up to a factor of two to demonstrate the effectiveness of flow control. VGJs were effective at maintaining approximately the same pitch-averaged total pressure loss with up

to half the total number of turbine blades. Alternatively, the blade shape itself can be modified to produce higher pressure loading with fewer blades. For example, considerable evidence suggests that front-loaded profiles experience lower separation losses.

1.3. The L1A LP Turbine Blade Profile

Another approach is to modify the blade shape itself to produce higher pressure loading with fewer blades. For example, Clark and Koch designed the L1M with the same flow angles as the Pack B (55 degree inlet angle, 30 degree exit angle), but with an increased spacing and loading [17]. By moving the peak C_p location from x/C_x = 0.65 to 0.47, the new blade is more mid-loaded than the Pack B. This new design achieved a Zweifel loading coefficient of 1.34 (17% higher than the Pack B), with no significant low Re loss down to Re = 10,000 [17,18]. The success of this redesign was consistent with a previous study by Praisner et al. [19] using front and aft loaded "Pack D" blade designs. Recently, McQuilling et al. [20] pushed the blade loading even higher (Zw = 1.6) with an L2F blade design that is more front loaded than the L1M but still preserves the flow angles of the Pack B design. Total pressure losses were maintained at a reduced level down to a Reynolds number of 15,000. By designing a turbine airfoil with the suction peak further upstream, the portion of the suction surface experiencing an adverse pressure gradient is extended, thereby reducing the risk of separation as well as leaving ample streamwise distance for reattachment [21]. Unfortunately, while front loading the pressure profile may be beneficial for mid-span profile losses, the early blade turning can aggravate losses in the endwall due to an elongated region experiencing an adverse pressure gradient and secondary flow migration (horseshoe, tip, and passage vortices). To avoid the highly three-dimensional (twisted) blade designs needed for optimal mid-span and endwall performance, aft-loaded designs incorporating some form of flow control are also of interest. Accordingly, this study focuses on the application of VGJ flow control to a new aft-loaded LPT profile (L1A) designed at AFRL.

The C_p predictions presented in this work were obtained within the AFRL Turbine Design and Analysis System (TDAAS), which was also used to design the L1A profile. The system was recently described in part by Clark and Grover [22], and it employs an industry-standard airfoil shape-generation algorithm developed in conjunction with design-optimization methods to define turbine blade and vane shapes. Time-resolved RANS analyses were performed using the grid generator and flow solver of Dorney and Davis [23], called "WILDCAT." The separated-flow transition model of Praisner and Clark [21] was used to predict the onset location of transition in the shear layer from the state of the boundary layer just prior to local flow reversal. Accordingly, point-wise trips were applied within the flow solver at the prescribed transition-onset locations. The C_p predictions were used for facility validation in the present study. It is noted that for steady flow at low Reynolds numbers the L1A experiences massive non-reattaching separation characterized by a rapidly transitioning free shear layer and laminar flow circulation on the majority of the aft portion of the blade. This contrasts many of its predecessors which exhibit flow reattachment downstream of separated shear layer transition, like the mid-loaded L1M (Zw = 1.34), or the aft-loaded Pack B (Zw = 1.15) [9,24]. As such the L1A serves as an excellent test bed to demonstrate the utility of VGJs.

1.4. Simulating Periodically Impinging Wakes

In order to better represent the unsteady flow field in the LPT environment, the interaction of impinging wakes with the suction side boundary layer has been investigated [14,25-32]. Numerous experimental investigations of wake-induced separated boundary layer transition have been conducted. Of the extensive body of literature available on the topic, several studies which were especially useful are cited herein to provide context for this work.

For example, in recent studies conducted by Reimann et al. [8], the dynamic response of the separated region on the suction surface of a Pack B LPT to each periodic wake passing and

pulsed VGJ disturbances was investigated using hot-film anemometry and PIV instrumentation. It was determined that the wake results in elevated turbulence levels and early breakdown of the separated shear layer, which energizes and flattens the boundary layer. Steiger et al. [29] attribute this effect to boundary layer embedded vortical structures, hypothesizing that these vortical structures were created by a rollup of the separated shear layer induced by the wake disturbance. In the case of the Pack B, the region of near-wall low-momentum fluid was thinned temporarily encouraging attached flow. Immediately following the wake disturbance, the boundary layer is characterized by a protracted "calmed zone" before reverting to the pre-wake separation extent. In many studies concerning wake interaction in the LPT it has been observed that a laminar-like calm zone ensues after the passing of the wake disturbance, and persists for several convective timescales. The calm zone combines the beneficial properties of both laminar and turbulent boundary layers due to reduced entropy generation and reduced receptivity to disturbances [8,14,33,34]. Furthermore, it has been observed that calmed zones contribute to a beneficial phase lag in the migration of boundary layer separation upstream to the steady state location. It is noteworthy that although the wake disturbance does modify the shear layer breakdown and amplify instabilities on the more highly loaded L1A, the heightened mixing does not reattach the boundary layer [9,24].

In a Pack-B low-speed linear cascade, Mahallati and Sjolander [30] performed phase-locked measurements using an array of surface-mounted hot-film anemometers to detect separation and reattachment and gain insight into the transitional condition of the boundary layer on the suction side of the Pack-B profile. Also, mid-span wake measurements were made with a hot-wire to assess the phase-locked velocity deficit in the wake of the Pack-B. Periodic wakes were shed into the test section using a spoked-wheel wake generator design located upstream of the cascade leading edge plane. Cylindrical bars are mounted radially outward on the large disk, so that the wake disturbance is essentially parallel to the spanwise direction of the two-

dimensional blade profile over several blade pitches. The flow coefficient ($\Phi = U_{in,axial}/U_{cyl}$) is easily varied by adjusting the bar speed and bar spacing. In addition to acquiring data at a variety of Reynolds numbers ranging from 25,000 – 100,000 (based on inlet velocity and axial chord), the linear wake bar speed and spacing were varied such that the impact of the wake forcing frequency and the flow coefficient could be evaluated. Worthy of note is the change in the bar wake's inclination (or incidence angle) as it enters the test section, due to a change in the relative velocity in the moving bar's frame of reference. Thus, a higher negative incidence is expected for lower flow coefficients. Moreover, aspects of the wake's distortion, due to the high strain exerted by the mean flow over the suction surface, are also expected for changes in wake orientation.

The surface hot-film results indicated an intensification of the free shear layer instability on the suction side of the blade while interacting with the wake disturbance. Turbulent patches which signify wake-induced transition were observed to develop in the area of the inflection point of the velocity profile in the separated free shear layer. A protracted calmed zone was observed evidenced by regions of depressed velocity fluctuation levels. With respect to wake forcing period, a threshold frequency was observed wherein the location of the boundary layer and transition onset did not have time to migrate upstream between wake events under the influence of the adverse pressure gradient. Furthermore, an optimal forcing frequency was identified which involved a compromise between separation bubble size and turbulent-wetted area. Consequently, the most beneficial parameter set for the wake-disturbance did not yield complete separation bubble elimination.

Schulte and Hodson [31] conducted similar experiments over a high lift LPT airfoil. Loss reductions were determined to be intimately linked to the relative portions of the blade surface covered by laminar, turbulent, calmed, and separated flow.

The addition of periodic impinging wakes to the flow field has been shown to bring about earlier flow transition, and separation of the turbulent boundary layer is consequently delayed.

Use of the notion of the *wake's negative jet* is frequently made throughout this work to interpret aspects of the blade-wake interaction. The notion was first conceived by Meyer [35]. Steiger and Hodson [34] investigated the interaction of periodic wakes with a separation bubble on the suction side of the T106 LP turbine profile. Experimental boundary layer measurements were made using a two-dimensional laser Doppler anemometry system phase-locked to a wake passing trigger. The negative jet is easily seen by plotting the perturbation velocity field, defined as the difference between the ensemble averaged and time-averaged velocity fields. Rendered in this fashion, the cylinder wake appears as a jet impinging on the blade surface and subsequently splitting into two streams. As the convecting jet interacts with the receptive separated shear layer, the forward-going stream (i.e. pointing downstream along the suction surface) increases the inflectional shape of the *total velocity profile* which corresponds to elevated velocity fluctuation as well. Regions of high vorticity are easily identified within the boundary layer, beneath this forward-going stream, and these regions are associated with vortices originating from the rollup of the shear layer. The backward-going stream has the opposite effect, and thus the shape of total streamwise velocity profiles alternates between inflectional and full. Steiger and Hodson concluded that the wake triggers a forced inviscid Kelvin-Helmholtz (K-H) rollup as it deforms the already unstable separated shear layer, and furthermore, that the rollup requires that there is a separated shear layer with which to contend.

Uzol et al. [26] performed a similar investigation on the same blade profile using Particle Image Velocimetry (PIV) instrumentation. Instantaneous images during wake interaction show a trail of small-scale vortices leading to the rollup of large-scale vortices in the separated shear layer. These structures appear to breakdown into smaller structures downstream, however, stronger than the upstream train of small vortices. The rollup structures play a critical role in transferring energy from the mean flow and redistributing the energy to the smaller length scales,

and thus the forced inviscid K-H instability mode is a very important aspect of wake-induced transition.

1.5. Shear Layers and the Kelvin-Helmholtz Instability Mode

Given the nature of the L1A separation at low Reynolds numbers, as well as the role of the K-H instability mode during wake-boundary layer interaction [26], it is relevant to address the development and consequence of large scale structures being shed from within boundary layer.

McAuliffe and Yaras [36] provide a comparative analysis of turbulent transition in planar free shear layers, separated shear layers (like those characteristic of separation bubbles on the suction side of LP turbine blades), and boundary layers in low disturbance environments. In each case, the transition of the layer may primarily occur via the inviscid Kelvin-Helmholtz instability mode, associated with the periodic shedding of vortical structures having the same sense as the layer. The most notable difference is the presence of a bounding surface, which gives rise to the notion of a dual mode instability. In the presence of a bounding wall, a separated shear layer exhibits two regions in which instabilities are characterized differently. Inviscid instability dominates the "outer" region, while viscous instability dominates the "inner" reverse-flow region. It was found that the distance of the velocity profile inflection point and the level of near-wall reverse flow dictate which instability mode is dominant. A free shear layer has considerably less damping than an attached boundary layer. It is most likely the lower damping of a free shear layer that is responsible for the shorter transition length in separated-flow transition.

McAuliffe and Yaras [37] discussed the role of the K-H instability mode in the transition process of separated shear layers, similar to those observed on LP turbine blades. A numerical investigation supported by experimental wind tunnel data was carried out for steady, low Re flow over a flat plate under the influence of a streamwise pressure gradient. Experimentally, the pressure gradient is imposed by a contoured wall which forms the ceiling of the test section.

Shear layer turbulent breakdown is described as occurring in regions of high shear between pairs of periodically shed spanwise-uniform vortical structures. The streamline curvature (or ripple), resulting from the shear layer receptivity to small perturbations, is amplified throughout the inviscidly unstable velocity field. The shear layer rollup is observed to occur in the same sense as the vorticity of the layer. At any streamwise measurement station, the peak unsteadiness in the separated shear layer is located near the inflection point of the ensemble-averaged velocity profile. Given the sense of the shear layer rollup, high-momentum flow is entrained toward the surface. The elevated wall-normal momentum exchange serves to reduce reverse flow levels as well as the inflectional shape of the velocity profiles. McAuliffe and Yaras also present a range of dimensionless Strouhal number, $Sr_{\theta s}$ (using momentum thickness and edge velocity at separation as characteristic length and velocity scales), which has been correlated to transition via the K-H instability. A variety of studies concerning separated shear layer, free shear layers, and boundary layers are included, and the all-encompassing range of Strouhal numbers reported is $0.008 < Sr_{\theta s} < 0.016$.

Volino [24] performed a steady state experimental analysis of the L1A at low Reynolds numbers. In this study, turbulent power spectra at six streamwise measurement locations from the suction peak to the trailing edge are presented to aid in the description of the separated shear layer transition process. At each streamwise location, spectra were acquired with a single-element hot-wire anemometer at the wall-normal coordinate where the maximum fluctuating velocity component was observed. Of particular relevance to the current study are the results presented for nominal exit Reynolds number (based on exit velocity and suction side length) of 50,000. (Note: This corresponds to an inlet Reynolds number (based on inlet velocity and axial chord) of 20,000.) For this Re, the spectra indicate a distinct, peak frequency of approximately 175Hz at the measurement station just downstream of the laminar separated shear layer extent. The remaining downstream measurement stations all show a broadband rise in power over the higher frequency

range, suggesting that the observed peak corresponds to the free shear layer instability, and that this mechanism initiates shear layer transition to turbulence. It is interesting to note that the Strouhal number, $Sr_{\theta s}$, calculated using the frequency peak, an appropriate approximation for boundary layer edge velocity, and the reported momentum thickness at separation (from the laminar boundary layer calculation using TEXSTAN [38]. For exit Reynolds numbers of 50,000 and 100,000 the calculated Strouhal number is between $0.010 < Sr_{\theta s} < 0.014$, which within the range of the Kelvin-Helmholtz instability mode correlations summarized by McAuliffe and Yaras [37].

1.6. The Present Study

The synchronous actuation of vortex generator jets (VGJs) with periodically impinging wakes is the subject of this study. A wake reduced forcing frequency (F_{red}) of 0.41 (f = 8.7Hz) was selected to be representative of engine operation. The *wake reduced frequency* ($F_{red} = f/(U_{ex}/c)$) is a parameter useful for considering the number of wake disturbances present during the interval of time required for a fluid particle to travel through the cascade passage. A value of F_{red} greater than one indicates that multiple disturbances are present in the passage simultaneously. The corresponding flow coefficient ($\Phi = U_{in,axial}/U_{cyl}$) is 0.91. Of particular interest are the effects of chord-wise location, frequency, and phase of VGJ implementation, as well as the phase lagged boundary layer response to these disturbances. In an effort to characterize the phase-lagged boundary layer response to wake and VGJ forcing, data are also presented with F_{red} reduced to 0.2. Detailed flow and pressure measurements (both time-averaged and phase locked) are presented for the case of unsteady wakes combined with VGJ flow control at two chordwise locations for this L1A blade profile. A spanwise row of VGJs was drilled into the acrylic L1A between the suction peak (58%C_x) and predicted natural separation. Previous studies of unsteady shear layer dynamics in response to periodic wake disturbances by Bons et al.

[9] showed that the time-mean separation moves to approximately 72%C_x. Furthermore, it was anticipated that VGJ pulsing at this downstream location in the presence of wakes may be as effective as the upstream location for similar blowing ratio, with the added benefit of a synergy due to synchronization with the wake passing. Thus, a row of VGJs was also drilled at this location, motivated by the hypothesis that equivalent improvements in cascade performance could be achieved and that VGJ mass flow savings may result from actuating nearer to the time-mean separation position and further exploiting the instability there. Moreover, the downstream location may, in fact, be the optimum site for flow control though it is well past the blade suction peak. The present study explores this hypothesis while varying the VGJ blowing ratio and phase. Parametric studies were conducted to determine the optimal timing and blowing ratio at each VGJ location. As a result of sensitivities observed in pressure measurements while employing pulsed VGJs at 72%C_x, this location is the primary focus for velocity data acquisition. Phase-locked single-element hot film data were acquired at a Reynolds number of 20,000 (based on axial chord and inlet velocity) for a variety of test conditions to temporally resolve the dynamic shear layer response to periodic wakes, and to optimal VGJ actuation between impinging wakes. Two-dimensional particle image velocimetry (PIV) data were also acquired in the same spanwise measurement plane as the hot-film data to investigate the temporal and spatial development of spanwise structures and assess their roles in achieving optimal separation flow control.

CHAPTER TWO: EXPERIMENTAL METHODS

2.1. Low-Speed Wind Tunnel

Data were taken using a low-speed open-loop wind tunnel powered by a centrifugal blower. Air passes through a series of flow straighteners to enter the test section of the tunnel with ±2% velocity uniformity and 0.3% freestream turbulence intensity. The inlet duct preceding the cascade inlet is square with a cross-sectional area of 0.239m^2 and is 1.52m long. Freestream turbulence at the cascade inlet plane is augmented to 3% using a square bar turbulence grid 1.35m (9.4C_x) upstream of the cascade inlet. The test section is constructed completely of acrylic to provide optical access. For a detailed description of the wind tunnel facility refer to Eldredge and Bons [39].

2.2. Test Section

2.2.1. L1A

The test section is a three-passage low-pressure turbine cascade with two fully immersed L1A blade profiles (Fig. 1). The L1A blades have an axial chord (C_x) of 0.143m and a true chord of 0.156m. The blade pitch (S) is 0.145m, thus a solidity (defined as the ratio of axial chord to blade pitch) of 0.99. The inlet and exit flow angles are 35° and 60°, respectively. The blade span is 0.38m. Data were acquired over the center 20% of the blade span, where the flow was shown to be approximately two-dimensional.

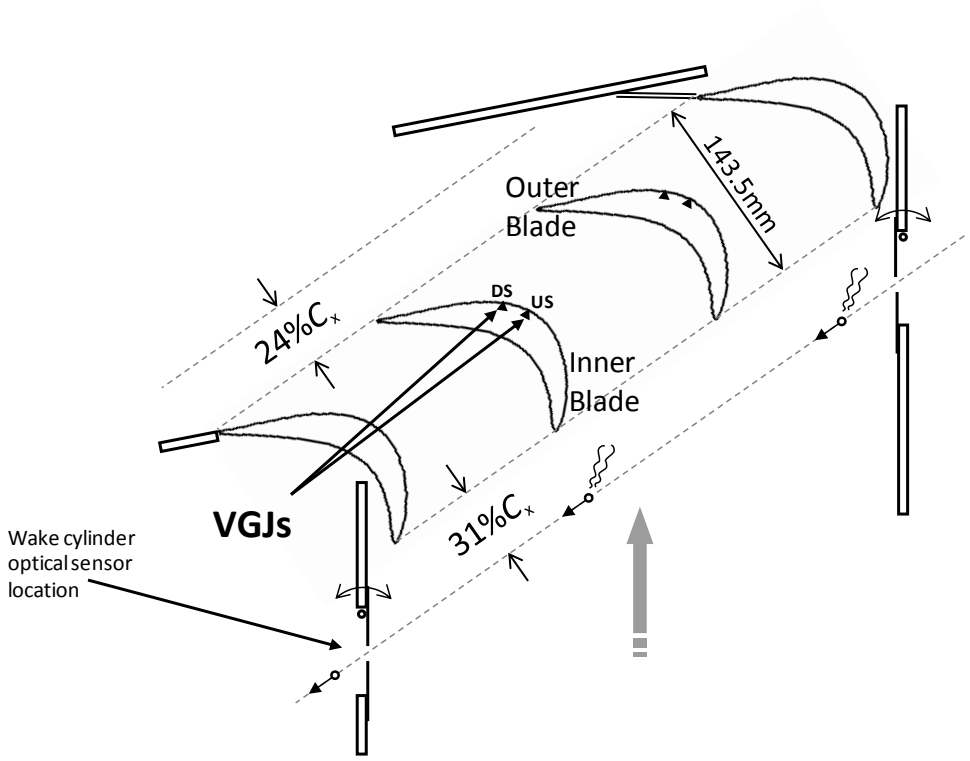

Figure 1: Schematic of L1A linear cascade. *Wake generator located 31%C_x upstream of cascade leading edge, wake total pressure surveys acquired 24%C_x downstream of cascade trailing edge plane.*

Each blade is equipped with 15 pressure taps on the suction surface and 7 taps on the pressure surface. The taps are 1mm in diameter and are waterfalled across the middle third of the blade span. These taps are connected to a 0.1"H_2O Druck differential pressure transducer to obtain the static pressure distribution along the blade surface. The C_p is calculated by dividing the difference of the inlet total pressure (from an upstream pitot-static probe) and local static pressure by the inlet dynamic pressure. The combined uncertainty in measured C_p data is less than ±8% at Re_c = 20,000. In order to acquire periodicity between the three passages, tailboards were needed to regulate the exit flow. Due to the character of the separation, positioning the outer tailboard to control the "uncovered" flow diffusion on the outer blade is more critical to producing periodicity at low Reynolds number. In addition to regulating the exit flow, peripheral inlet bleeds metered

by flaps (shown in Fig. 1) are used to adjust blade loading until the C_p data indicate good agreement between the two immersed blades. As with the tailboards, the blade loading is more sensitive to the flow area of the outer inlet bleed. With regard to the present work, periodicity is first acquired for an attached flow condition (e.g. $Re_c \approx 60{,}000$) using the prediction [22] as a guide, and then periodicity is validated at through a range of Reynolds numbers down to 20,000.

The L1A is an aft-loaded blade profile with a design Zweifel coefficient of 1.34 and suction peak at about 58%C_x. Figure 5 shows the C_p distribution for the two immersed blades (designated "inner" and "outer" as shown in Fig.1) through multiple Reynolds numbers. At low Reynolds numbers, the blades exhibits a massive natural separation beginning at approximately 59%C_x and continuing off the trailing edge of the blade. Although various factors affect separation and transition, flow reattachment is typically observed as a result of transition occurring in the separated shear layer above the separation [9,24]. Evidently, the strong curvature near the suction peak inhibits reattachment due to separated flow transition.

2.2.2. Wake Generator

The test section is also equipped with a wake generator upstream of the cascade inlet plane, shown in Figs. 1 and 2. The wake generator is designed to simulate the unsteady passage of an upstream blade row within the turbine. Periodic wake disturbances are shed into the test section by traversing circular carbon-fiber cylinders (diameter, D = 4mm) through the incoming flow along a plane parallel to the inlet plane and 11D (0.31C_x) upstream of the cascade leading edge. The cylinder diameter and location were selected to simulate the velocity deficit in the wake of an upstream turbine vane with attached boundary layers. The spanwise-oriented cylinders are mounted on a chain-sprocket assembly which is driven by a variable frequency motor.

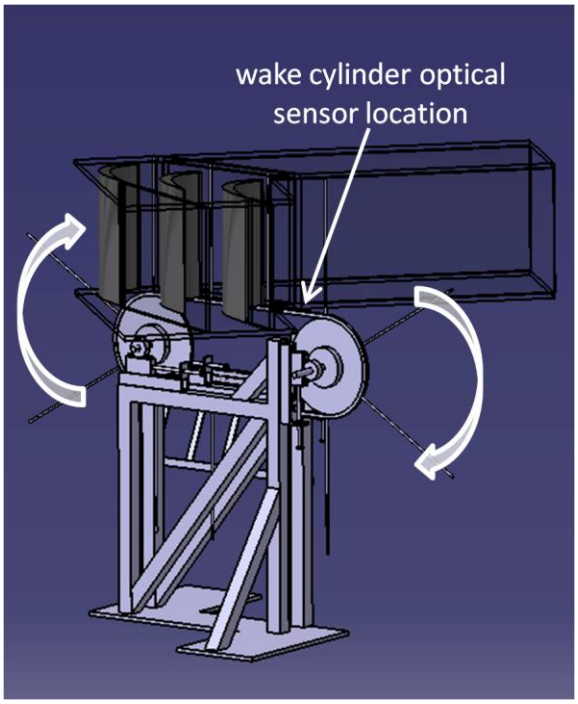

Figure 2: CAD model of wake generator and test section of tunnel. *Wake generator located 31%C_x upstream of cascade leading edge. Curved white arrows indicate direction of rotation. Straight arrow points to location of optical sensor.*

The linear speed of the cylinders (U_{cyl}) is maintained to yield a prescribed flow coefficient ($\Phi = U_{in,axial}/U_{cyl}$) with a fluctuation of approximately ±2%. For the present work, the flow coefficient of 0.91 is selected in accord with typical engine conditions. Cylinder spacing was varied to study the effect of forcing frequency while maintaining a constant flow coefficient. The cylinders are initially spaced 0.229m apart. The cylinder spacing is 57% larger than the blade spacing. This is to yield an approximate equivalent of a rotor-stator pitch ratio as there are typically 30-40% fewer stator vanes than rotor blades for a given low-pressure turbine stage. The frequency is subsequently decreased by removing alternate cylinders on the chain, thereby increasing the cylinder spacing to 0.458m. The cases with all cylinders and with dropped cylinders correspond to wake reduced frequencies ($F_{red} = f/(U_{ex}/c)$) of 0.41 and 0.20, respectively.

Brushes lining all four sides of the cross-section serve to dampen cylinder vibrations as well as seal the wind tunnel. An optical sensor is used to signal the passing of each cylinder as it exits the tunnel (see note in Fig. 1). For a more detailed description of the wake generator see Bloxham et al. [14].

2.2.3. Vortex Generator Jets

Flow control is performed by use of a spanwise row of vortex generating jets (VGJs). A spanwise plenum feeds pressurized air to VGJs on both immersed blades. The cylindrical jets are 2.6mm in diameter (d) and are spaced 10d apart. The current study involves the evaluation of two rows of VGJs installed in each of the two immersed blades, located at 59% (upstream = US) and 72%C_x (downstream = DS) as shown in Fig. 1. VGJs are typically configured with a low pitch angle and aggressive skew angle to produce a single, dominant, slowly-decaying streamwise vortex. To comply with this, the jet fluid is injected with a 30° pitch angle to the blade surface and a 90° skew angle to the streamwise direction (see inset of Fig. 3). Each plenum is connected to high pressure air with an inline Parker-Hannifin high-speed solenoid valve that regulates the VGJ exit velocity. A General Valve Inc. Iota One pulse driver is used to set the duration of the VGJ pulse and the time of actuation relative to the input signal from the cylinder sensor (t = 0). The valve is synchronized to the passing of the wake generating cylinders (8.7Hz for the all-cylinder case and 4.35Hz for the dropped-cylinder case) and operated at a 25% duty cycle (29ms "on") based on the 115ms period (T) of the all-cylinder case (12.5% duty cycle for the dropped-cylinder case). Since the VGJs are synchronized to the cylinder passing frequency, this wake period yields a dimensionless forcing frequency of $F^+ = 0.2$ for this study (based on the distance from the VGJs to the blade trailing edge, SSLJ, and the mean passage velocity, U_{avg}). The jet velocity is adjusted with an inline pressure regulator.

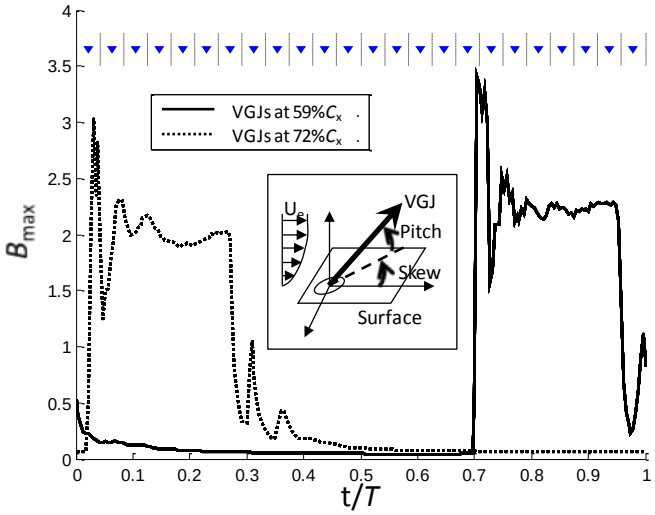

Figure 3: Pulsed VGJ blowing ratio plotted against dimensionless time. *VGJs at 59% and 72%C_x; indicating the implemented phase of VGJ actuation with respect to the wake sensor; t/T = 0 corresponds to signal from optical wake cylinder sensor; blue triangles indicate the center of 24 measurement phases for phase-locked data acquisition.*

The ensemble-averaged pulse jet signatures (at 59%C_x and 72%C_x) were measured with a single-element hot-film (hot-film length ≈ 40%d) located at the hole exit while injecting into quiescent surroundings. Though not presented, measurements made at several midspan VGJs indicated that the VGJ disturbance is spanwise uniform across the middle third of each immersed blade. Furthermore, the high-pressure air flow is divided equally between the two blades. The local freestream velocity was calculated from the local pressure coefficient at the respective VGJ site. The jet profiles for the two VGJ locations are provided in Fig. 3 (Note: the signal from the wake cylinder sensor corresponds to $t/T = 0$). The phase of VGJ actuation implemented at each control location is indicated. VGJ actuation at 59% and 72%C_x is initiated 0.70T and 0.02T, respectively, after the pulse driver receives the signal from the wake generator. The peak unsteady jet velocity (U_{jet}) was fixed to yield a blowing ratio ($B_{max} = U_{jet}/U_{e,local}$) of 2 for both rows of jets (unless otherwise indicated). However, there is a significant overshoot ($B_{max} \geq 3$) for

both rows of VGJs due to non-ideal feed plenum dynamics. VGJ actuation was always implemented on both blades simultaneously.

2.3. Data Acquisition and Processing

2.3.1. Integrated Wake Loss (γ_{int})

A Type KBC United Sensor Kiel probe was used to measure the total pressure loss (referenced to an upstream pitot probe) through the wake of the inner blade. The outer diameter of the sensing head is 3.175mm and the time constant is 15 seconds. The probe accurately measures total pressure within pitch and yaw ranges of ±45° with respect to the approaching flow direction. The sensing head of the probe was positioned at mid-span and traversed in a plane parallel to the cascade exit and 35 mm (24%C_x) downstream as illustrated in Fig. 1. The integrated wake loss coefficient is a measure of the changes in total pressure, and thus momentum, caused by viscous losses and mixing in the boundary layer. In this study the parameter is non-dimensionalized by the blade pitch (S) to create an area-averaged loss parameter given by Eqn. 1.

$$\gamma_{\text{int}} = \frac{1}{S}\int_{-S/2}^{S/2}\left(\frac{P_{T,in} - P_{T,ex}}{P_{T,in} - P_{S,in}}\right)ds \qquad \text{Eqn. 1}$$

Prior to taking phase-locked velocity data, the blowing ratio and time delay (between the optical sensor signal and VGJ actuation) were optimized to achieve the greatest reduction in wake total pressure loss. γ_{int} values were used to measure the impact of these parameters and make the appropriate selection.

2.3.2. Hot-film Velocity Measurements

Unsteady velocity data were acquired using a single sensor hot-film anemometer (TSI model 1210-20) which was mounted to a 3-axis traverse above the cascade. The film is 50.8μm in diameter, 1.02mm long, and has a maximum frequency response below 100kHz. This device has

a calibration uncertainty of ±0.08m/s at a typical passage velocity of 5m/s. The hot-film signal was low-pass filtered at 10kHz to attenuate noise. A spring-loaded follower device is used to traverse the film along the blade surface at a specific wall normal distance (y/C_x). The anemometer was traversed along the blade surface multiple times, each at a different distance from the wall ranging from $0.014 < y/C_x < 0.086$. The uncertainty in the distance from the wall was ±0.2 mm. Data profiles were acquired at 60 streamwise locations, each ranging 2-5 mm apart. Measurements were concentrated in regions where separation was expected to occur. Five different cases were investigated with this "follower" approach including the following cases: steady state, wakes only at F_{red} =0.41 and 0.20, and wakes + VGJs at 72%C_x for F_{red} = 0.41 and 0.20 (the corresponding reduced VGJ forcing frequencies are F^+ = 0.2 and F^+ = 0.1, respectively).

Data were processed to higher order turbulence statistics and intermittency following the process outlined in Bons et al. [40]. For the steady state case, data were acquired for 15sec, sampling at 10kHz. For the data collected using the wake generator, data acquisition was phase locked to the cylinder exit sensor, each sensor pulse constituting one cycle. For the cases wherein F_{red} = 0.4, data were acquired at 10kHz for 20sec at each follower position, allowing for 173 wake passing cycles. For F_{red} = 0.2, 25sec of data were acquired at the same rate to capture 108 wake passing cycles. At each wall-normal position, all of the wake passing cycles are averaged together to produce an ensemble average mean velocity profile for each cycle. This ensemble average is then subtracted from each individual cycle in order to eliminate the bulk unsteady motion of the flow and proceed with statistical calculations. Each cycle is then split into 24 or 48 equal phases for the F_{red} = 0.4 and F_{red} = 0.2 cases, respectively, in order to maintain the temporal resolution of each phase. Finally, the first phases of each cycle were concatenated together and turbulence statistics were determined. This concatenation process was repeated for the remaining phases of each cycle. The wake passing periods (cycle periods) are T=115ms and 230ms for F_{red} = 0.41 and 0.20, respectively.

2.3.3. Particle Image Velocimetry

Two-dimensional velocity data were taken using a single-camera LaVision particle image velocimetry (PIV) system. The high speed camera (resolution of 1376 by 1040 pixels) was mounted to a three-axis traverse atop the test section. The camera window was oriented to capture the interaction of periodically impinging wakes and the separated flow on the aft portion of the inner blade suction surface. The data window covered the portion of the inner blade between approximately 50% and 90%C_x (see Fig. 4) where the blade surface is mostly flat. The camera orientation is such that the camera coordinates (x,y) are approximately aligned with the streamwise and wall-normal blade coordinates, and PIV data is presented in the camera coordinate system.

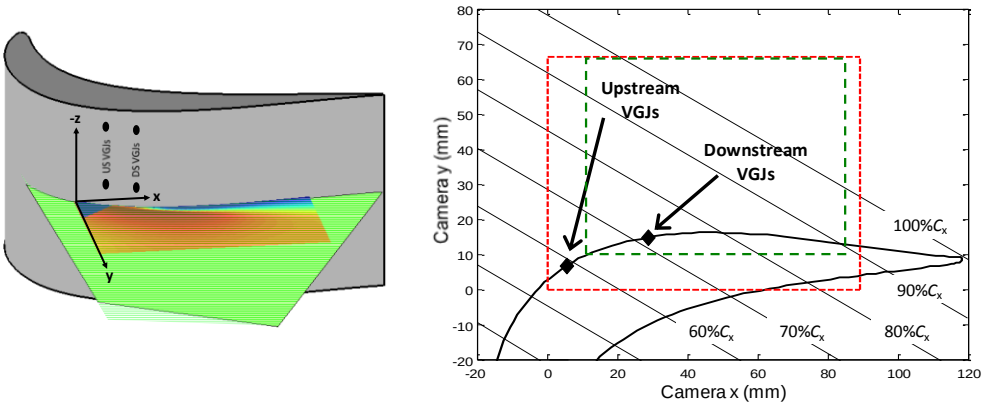

Figure 4: The data collection region (left) and coordinate system used to present 2-D PIV data (right). *Left: the green plane represents the laser sheet, located 4d below the top of a midspan VGJ. Right: the dashed red line represents the PIV camera measurement window; the dashed green line indicates the cropped window for data presented herein; also included are the axial chord lines for the L1A.*

A Nd:YAG laser mounted to a three-axis traverse on one side of the test section was used to project two consecutive 1mm thick laser sheets (with a 100μs time separation) in the x-y plane into the test section (see Fig. 4 for coordinate system). The flow was seeded with olive oil

particles having diameters between 1 and 2μm. The high-speed digital camera is synchronized with the laser pulses to capture two exposures of the light scattered by the olive oil particulate. Each double-exposure was phase-locked to begin at a specified time delay after being triggered by the wake-passing sensor. The wake-passing period (T) of 115ms was divided into 24 equal segments to mimic the procedure for data acquired with the hot-film. Each segment was phase locked to the passing of the cylinder using the optical sensor. Figure 3 shows the 24 non-dimensional instants when PIV data were acquired (recall that $t/T = 0$ corresponds to the cylinder passing through the optical sensor). The initial dataset was collected at $t/T = 0.0208$. The subsequent datasets were taken 4.8ms apart ($\Delta t/T = 0.0417$). Typically, one thousand images are sufficient for the convergence of turbulence statistics. Results of a convergence study indicate that six hundred images are sufficient for the present study. Thus, eight hundred images were acquired, processed and averaged for each measurement phase to conserve disk space. Interrogation windows of 16 pixels by 16 pixels which overlap one another by 50% were used to compute spatial correlation and output velocity vectors. According to LaVision [41], for an average particle displacement of 8 pixels, uncertainty in the seed particle displacement is approximately 0.2 pixels. This translates to a velocity uncertainty of ±0.08 m/s. Measurements were taken at a single spanwise (z) location, 4d below midspan VGJ (as shown in Fig. 4), where the flow was shown to be spanwise uniform and seed remains in the plane of the laser sheet. (Note: The hot-film and PIV data planes do approximately coincide.)

CHAPTER THREE: RESULTS AND DISCUSSION

A summary of the steady state results at low Reynolds numbers is provided first, followed by the characterization of VGJ synchronization at two strategic chordwise VGJ locations. Several unsteady cases which primarily focus on the synchronous application of the *downstream* VGJs with upstream wakes are presented. Phase-locked one-dimensional velocity data measured with a single-element hot-film is presented first. The presentation of 1-D unsteady data begins with the unsteady baseline (case I) wherein the flow is modified by wakes alone (no jets), followed by the case with optimal VGJ actuation at 72%C_x synchronized with passing wakes (case II). For these two cases the *wake reduced frequency* (F_{red}) is 0.41, and the flow coefficient (Φ) is 0.91. Two similar cases are then presented (cases III and IV) wherein the F_{red} was reduced to 0.20. The flow coefficient is maintained by fixing the wake generator cylinder speed (U_{cyl} = 1.99m/s) and removing alternate cylinders. Ramifications of the observed separated shear layer position with regard to jet penetration are discussed.

Two-dimensional phase-locked PIV velocity data is presented for cases I and II. First the *wake-only* case is presented and the notion of the wake's negative jet is discussed. Finally, the application of VGJ separation control with unsteady wakes is presented, and the mechanisms resulting in enhanced cascade performance are discussed in detail.

3.1. Steady State L1A (No Wakes, No VGJs)

Figure 5 shows both the predicted and measured C_p distribution for the L1A profile at three Reynolds numbers. The steady state predictions for the L1A are a product of the

aforementioned AFRL design code [22]. The tailboards and peripheral inlet bleeds of the cascade were appropriately adjusted to yield approximately the same C_p distribution on the two blades. At all three Reynolds numbers, the experimental data match the prediction very well. For lower Reynolds numbers, the lower suction peak (4.2 as compared with the design value of 5.3) and the pressure plateau for $x/C_x > 0.6$ are characteristics of a massively separated blade profile. For the $Re_c = 60{,}000$ case, the measured suction peak coincides with the predicted location ($x/C_x \approx 0.6$), but the C_p values are slightly higher than the prediction for the entire forward portion of the blade ($x/C_x < 0.5$) and slightly lower than the prediction for $x/C_x > 0.8$. The predicted separation bubble at $x/C_x = 0.75$ is not evident from the experimental data due to the lack of pressure taps in this region. However, flow visualization performed with thin smoke wire reveal a short, thin separation zone from 70% - 75%C_x.

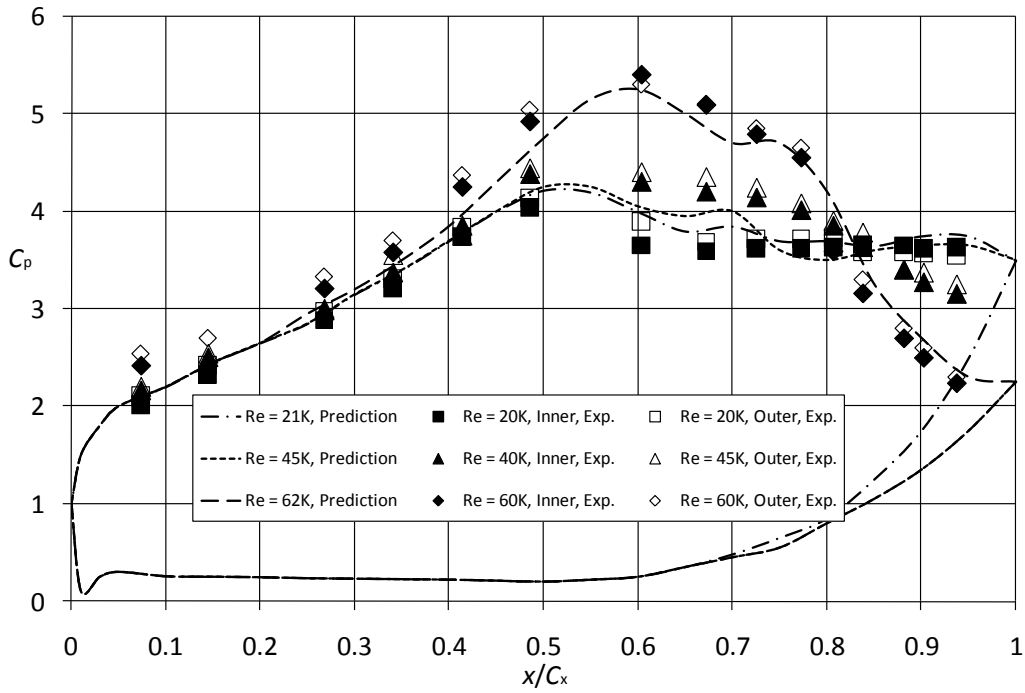

Figure 5: Predicted [22] and measured (Exp.) C_p values for immersed L1A blades at three Reynolds numbers. *The designation "inner" and "outer" is consistent with Fig. 1.*

It is instructive to compare the difference in blade loading between attached and separated flow cases. For example, if the experimental blade was a turbine rotor, the elevated suction peak of the L1A cascade for $Re_c \approx 60{,}000$ would yield an increase in the work available for $Re_c \approx 20{,}000$ due to a larger integrated pressure force in the direction of rotation. Specifically, comparing the blade loading parameter (ψ) defined in Eqn. 2, it is determined that the blade loading for the $Re_c \approx 20{,}000$ prediction in Fig. 5 is 20% less than that calculated from the $Re_c \approx 60{,}000$ prediction, and this represents the opportunity for improved work extraction with the introduction of unsteady wakes and VGJs.

$$\psi = \int_{blade} \left(\frac{P_{T,in} - P_{S,local}}{P_{T,in}} \right) \frac{\hat{e}_n \cdot \hat{e}_t}{c} ds \qquad \text{Eqn. 2}$$

The area-averaged wake total pressure loss (γ_{int}) data are compared to the corresponding prediction in Fig. 6. The losses rise dramatically for $Re_c < 50{,}000$, with the experimental and predicted values matching within 20% for $Re_c > 50{,}000$. The predicted loss levels out below $Re_c = 50{,}000$ while the measurements show a steep rise to just under two times the predicted value at $Re_c = 20{,}000$. The underpredicted loss at very low Re is consistent with results from previous studies [9,24]. The exaggerated magnitude of the wake total pressure loss at low Re_c also make the L1A cascade an ideal candidate for control, since there is significant room for improving γ_{int} as well.

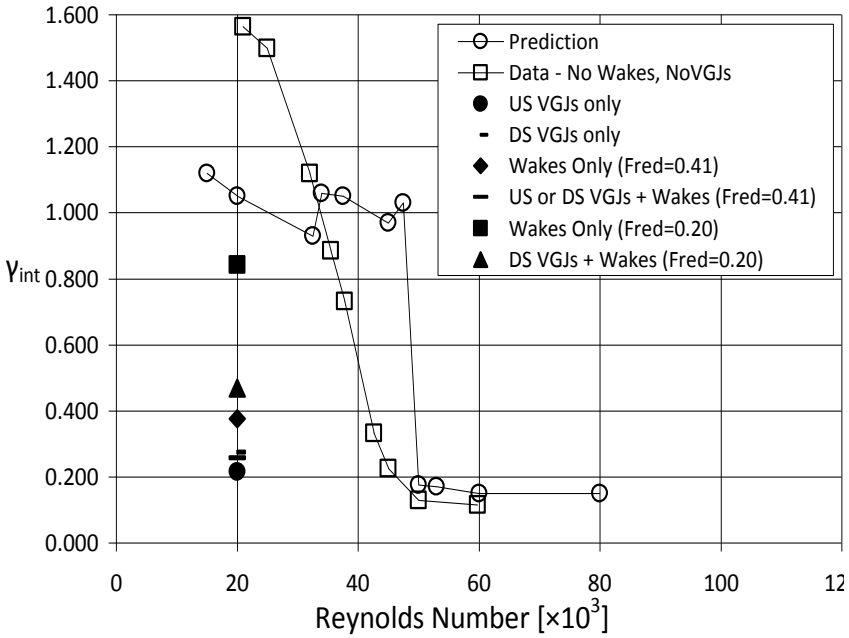

Figure 6: Predicted [22] and measured area-averaged wake total pressure loss (γ_{int}) vs. Reynolds number for L1A.

Figure 7 includes contour plots of u_{mean}/U_{in}, u_{rms}/U_{in}, and intermittency for the steady state boundary layer at $Re_c \approx 20{,}000$. The data are presented with the wall normal distance from the suction side along the ordinate and axial chord location indicated on the abscissa. The locations of separation and shear layer transition are noted. In the absence of a wall shear measurement to precisely identify the separation location, it was determined from Fig. 7 that the point of incipient separation is near 60%C_x. This is identified in the plots by the region of rising near wall u_{rms} accompanied by the sharp drop-off in u_{mean} that occurs as the boundary layer becomes a separated free shear layer. Following separation, the region of rising turbulence lifts away from the wall and forms a separated free shear layer above a region of unsteady reverse near-wall fluid. After a short distance, this laminar shear layer begins to transition to a turbulent shear layer. As identified in the plots, turbulent breakdown occurs at approximately 66%C_x for the L1A. Contours of intermittency indicate the percent of turbulent fluctuation in a hot-film data sample, and thus

intermittency is frequently used as a transition indicator. In Fig. 7, it is noted that the location of transition occurs in the region of the shear layer breakdown. Based on these results the laminar free shear layer extent is 6%C_x.

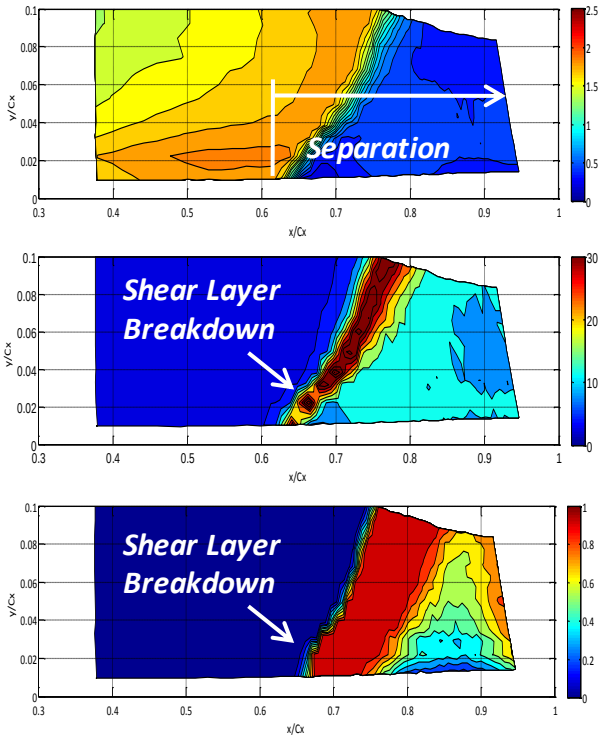

Figure 7: Hot-film results for steady state boundary layer of the L1A at Re_c = 20,000. *Contour plots of u_{mean}/U_{in} (top), u_{rms}/U_{in} [%] (middle), and intermittency (bottom) presented in wall normal vs. axial chord coordinates.*

Figure 8 plots the acceleration parameter (K) on the suction surface of the L1A, calculated according to Eqn. 3, using the measured and predicted C_p distributions at $Re_c \approx 60{,}000$.

$$K = \nu \frac{dU_e}{dx} \frac{1}{U_e^2} \qquad \text{Eqn. 3}$$

The design K profile presented in Fig. 8 shows that the passage flow experiences aggressive diffusion (K<0) due to the curvature of the L1A blade profile. The minimum design

value near the suction peak ($x/C_x \approx 0.6$) is approximately -1.25×10^{-6} and downstream of the suction peak $-0.625 \times 10^{-6} < K < -2.5 \times 10^{-6}$. The design values reported by Bons et al. [9] and Volino [24] for the L1M and the Pack B (a couple predecessors of the L1A) are compared here to provide context for the heightened diffusion to which the L1A passage flow is subjected. Both sources indicate comparable minimum K values near respective suction peaks. The acceleration parameter downstream of the suction peaks for both the L1M and Pack B are not as adverse as $K \approx -1.25 \times 10^{-6}$. A cubic spline fit was applied to the measured C_p distribution ($Re_c = 60{,}000$) in Fig. 5 to estimate the acceleration parameter for the current L1A cascade configuration. Compared to the periodic calculation, the cascade exhibits an elevated level of diffusion on the aft portion of the suction surface. Rapid transition is expected due to the strong, destabilizing adverse pressure gradient and aggressive diffusion experienced by the mean flow as noted in the C_p profile. By comparing the Pack B and the L1A measurements, Bons et al. surmised that the proximity of the separated shear layer to the wall appears to play a role in determining if the wake disturbance field causes a reattachment (Pack B) or not (L1A). When the separated shear layer is too far removed from the blade surface, the free shear layer unsteadiness is not able to penetrate down to the wall and fails to effectively reenergize the near wall (separated) fluid.

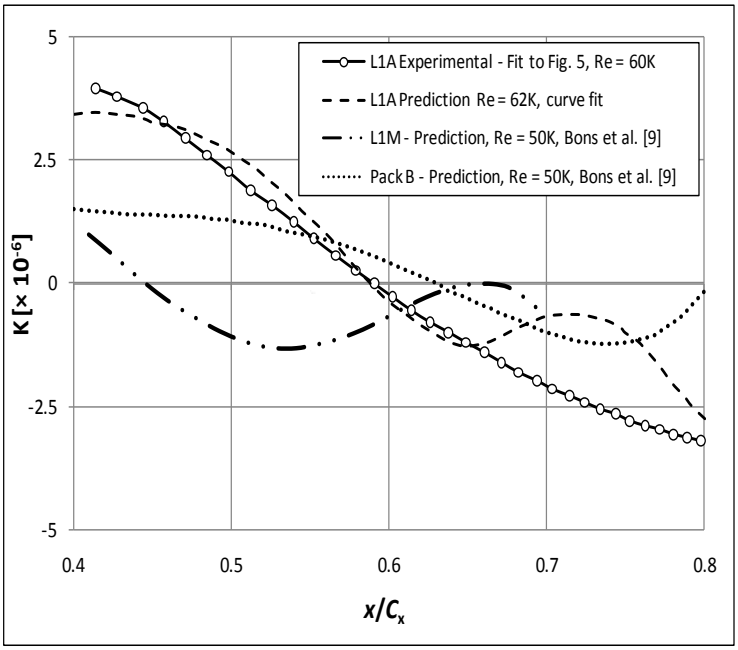

Figure 8: Suction surface acceleration parameter plotted against x/C_x. *Calculated from predicted and measured C_p data in Fig. 5 (*Re_c *= 60,000).*

Under steady conditions the shear layer breakdown does not spread down toward the wall, unlike the L1A's predecessors. The free shear layer breakdown occurs in a region of the blade with such strong curvature (Fig. 8) that the heightened mixing never manages to propagate down through the separation bubble to reattach the flow. The entire aft portion of the blade is characterized by unsteady flow circulation which explains the excessive wake loss values at low Reynolds numbers shown in Fig. 6.

The steady state shear layer position for Re_c = 20,000 is included with the time-averaged results of the unsteady cases in Fig. 9 to aid in describing shear layer displacement and orientation. The solid and dashed lines in the figure are constant curves of u_{rms}/U_{in} = 15% extracted from contour plots in the format of Fig. 7. Constant curves of u_{rms}/U_{in} = 10% and 20% were also extracted from the data to form the upstream and downstream boundaries respectively

of the locus of points encompassing each time-averaged shear layer. Each curve was approximated with either a second or third degree polynomial fit.

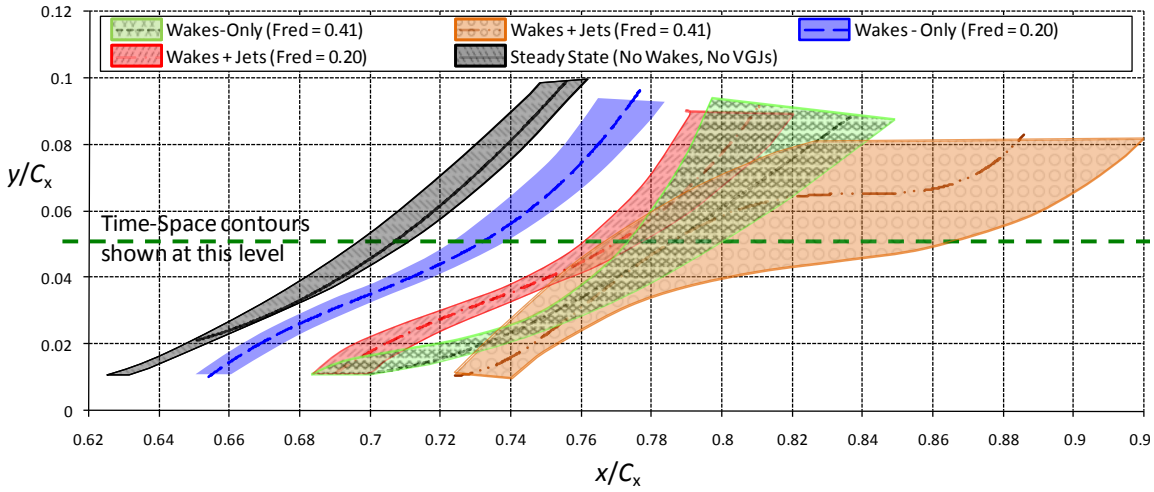

Figure 9: Time-averaged shear layer comparison. *Data shown for steady state, wake-only (F_{red} = 0.41 & 0.20), and wake + VGJ actuation at 72%C_x (F_{red} = 0.41 & 0.20) cases. Upstream and downstream boundaries formed by constant curves of u_{rms}/U_{in} = 10% and 20% respectively. The solid or dashed line between boundaries formed by constant curves of u_{rms}/U_{in} = 15%.* Re_c = *20,000.*

3.2. L1A with Unsteady Wakes + VGJs

3.2.1. C_p and γ_{int} Analysis of VGJ Synchronization and Chordwise Location

Each of the two immersed blades in the L1A cascade is outfitted with two spanwise rows of VGJs. The upstream (US) row is located at 59%C_x near the location of the blade's incipient separation under steady flow conditions and Re_c = 20,000. The downstream (DS) row is located near the blade profile's average location of incipient separation with unsteady wakes alone (72%C_x). Figure 10 shows the C_p profiles on the inner blade for steady conditions, with unsteady wakes only, and with synchronous VGJ actuation between wake events at both axial locations.

Each row of VGJs was operated at a duty cycle of 25% and $B_{max} \approx 2$. The wake cylinder flow coefficient was maintained at 0.91, and the wake reduced frequency, F_{red}, is 0.41.

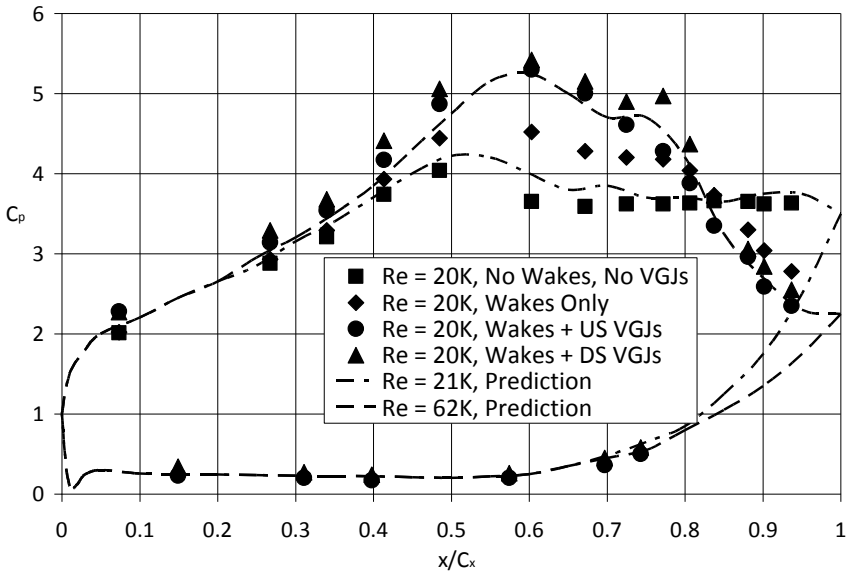

Figure 10: C_p data for steady state, wakes, wakes + upstream VGJ, and wakes + downstream VGJ cases at Re_c = 20,000 compared to prediction for L1A.

By inspection of Figs. 6 and 10, pulsed VGJs at either location are capable of recovering the attached flow diffusion experienced by the L1A at high Reynolds numbers, correcting the separation to a greater extent than do wakes alone. A plateau between $0.70 < x/C_x < 0.75$ is more pronounced in the C_p profile acquired with the VGJs at 72%C_x. In an average sense this is an indication of local deceleration, which is not present when actuating at the upstream location. The benefits of synchronous actuation are also evident in the integrated wake total pressure loss (Fig. 6). A 35% improvement in γ_{int} over the wakes-only case is achieved by actuating at either location, and the integrated loss is similar to levels observed for $Re_c > 50{,}000$.

In previous studies with the Pack B [14] it was reported that the separation bubble size was minimized for an optimum synchronization of VGJs and wakes with the jet being activated

precisely between consecutive wakes (just before the wake-induced calm zone reverts to a state of elevated velocity fluctuation, u_{rms}). For the L1A, Bons et al. [9] previously concluded that while phase of actuation was not important when actuating upstream, alignment of the jet pulse between wake events was critical to achieving optimal performance when actuating downstream. For the present investigation, a similar study was conducted wherein the relative timing of the two events was varied in $t/T \approx 0.07$ increments. Figure 11 shows the integrated wake loss measurements normalized by the wake loss value with wakes only. (Thus, a value of unity indicates no effect of flow control.)

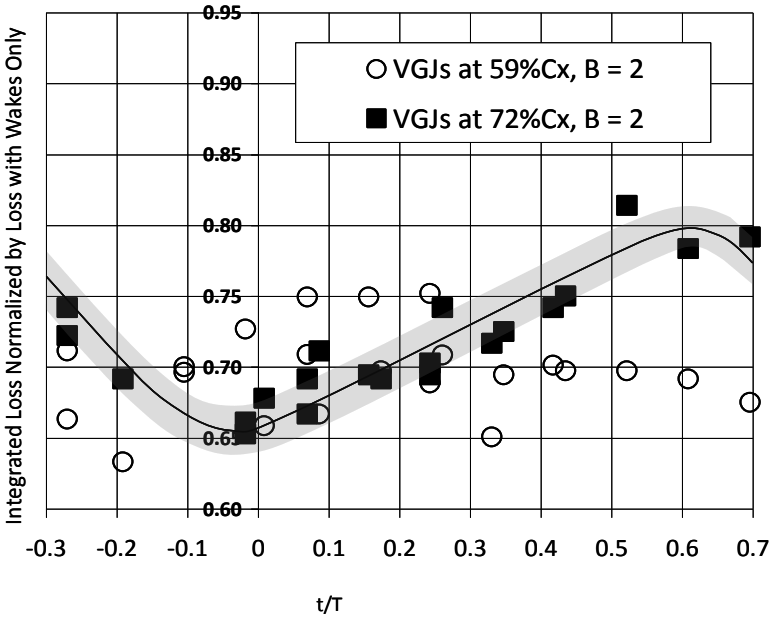

Figure 11: Wake total pressure loss normalized by loss with wakes only, plotted against dimensionless time. Data for VGJ actuation at 59% and 72%C_x. Re_c *= 20,000,* F_{red} *= 0.41,* B_{max} *= 2. The abscissa is actuation time non-dimensionalized by the wake passing period, where* t/T *= 0 is the time that each wake cylinder passes the optical sensor as it exits the cascade.*

For the upstream VGJ location, the data show no significant optimum with regard to synchronization. In fact, the integrated wake loss was approximately the same whether the VGJs

were employed with or without unsteady wakes (Fig. 6). On the other hand, actuation at the downstream VGJ location (72%C_x) does show a significant effect of synchronization. The loss minimum in Fig. 11 occurs for $0.90 < t/T < 0$, and the loss maximum occurs for $0.55 < t/T < 0.65$, approximately 60% later (or 40% earlier) in the wake passing period. (Note: the data previously shown in Figs. 6 and 10 were acquired actuating at $t/T = 0$ with downstream jets and at $t/T = 0.7$ with upstream jets. This was selected based on the fluid particle transit time between 59% and 72%C_x, approximately $t/T = 0.2$.)

3.2.2. Hot-film Velocity Data Analysis for two Forcing Frequencies

I. Wakes Only (No VGJs), $F_{red} = 0.41$

When wakes alone are introduced into the inlet plane of the cascade, the time-averaged C_p distribution shows an immediate benefit (Fig. 10). The peak C_p approaches 4.5 and the time-averaged separation is reduced considerably. Unsteady excitation by upstream wakes alone also reduces the wake total pressure loss downstream of the cascade trailing edge (γ_{int} measured at 24%C_x) to approximately 0.4 (less than a quarter of the steady state value at $Re_c = 20{,}000$) as indicated in Fig. 6. It is noted that for cases including unsteady wakes, the γ_{int} values reported do not isolate total pressure loss due to viscous mixing in the boundary layer from pressure loss inherent to wake generation (i.e. *background* pressure loss in γ_{int} wake surveys).

During unsteady operation (ie. with wakes or unsteady jets) the separation zone and shear layer positions have been described in previous studies as residing in a quasi-stable equilibrium position shifted downstream of the steady state position, with a substantial reduction in the separation size. In these studies, the relevant forcing frequencies are high enough to capitalize on the "calmed zones" which have been shown to ensue after a spanwise wake or discrete jet disturbance. Given the periodic nature of the disturbances, it is convenient to interpret temporally resolved velocity data as an average velocity field ($u_{cycleavg}$) superposed with a perturbation velocity field (Δu_{mean}). Figure 12 depicts the data reduction (in the format of Fig. 7) which amounts to subtracting the cycle average normalized velocity field (case-specific) from each

phase of the time-resolved u_{mean}/U_{in} data. Therefore, a positive magnitude in the perturbation velocity field indicates an increase in the u_{mean} velocity field with respect to the cycle average.

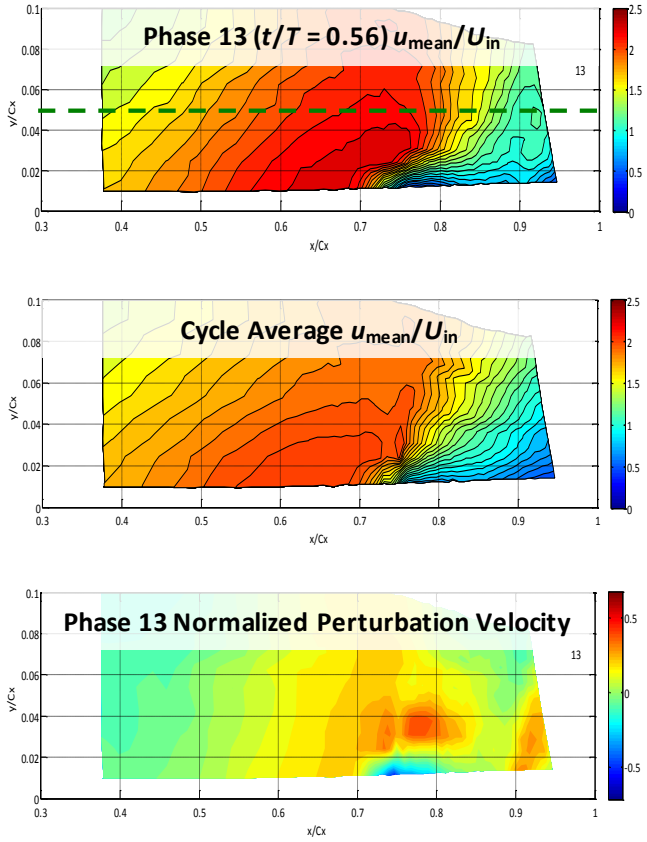

Figure 12: Depiction of perturbation velocity field formulation. *Phase-locked u_{mean}/U_{in} data shown for phase 13 of 24 (top) minus the cycle average u_{mean}/U_{in} data (middle) yields the normalized perturbation velocity field of phase 13. The dashed green line on the u_{mean} plot at y/C_x = 0.05 is the wall normal level shown in the time-space plots in later figures.*

Figure 13 shows the phase-locked u_{rms}/U_{in} and $\Delta u_{mean}/U_{in}$ data for 24 discrete phases through the wake passing period in the same format as Fig. 6. Evidenced by elevated u_{rms} fluctuations (Fig. 13a), the wake is present in the domain between $0.48 < t/T < 0.98$. Between $0.02 < t/T < 0.19$, the almost negligible perturbation velocity field (Fig. 13b) indicates that the mean velocity field is nearly identical to the cycle average. The wake is preceded by a significant

positive Δu_{mean} perturbation. The perturbation is present over the interval $0.27 < t/T < 0.60$ and reaches a maximum value of $\Delta u_{mean}/U_{in} \approx 0.35$ ($t/T = 0.56$) as it amplifies unsteadiness in the shear layer indicated by increasing u_{rms} over the same interval. In Fig. 13b, at $t/T = 0.52$, and $x/C_x = 0.75$ and $y/C_x = 0.06$, the local acceleration is convecting above the separated shear layer. The acceleration is followed immediately by the cylinder wake, with lower velocity and elevated u_{rms} (5% as compared with <1%). In Fig. 13b, the bar wake itself is visible as a negative perturbation velocity. The separated shear layer is gradually destabilized by the elevated turbulence and a tongue of elevated u_{rms} projects upstream from (x/C_x=0.75, y/C_x=0.03) to (x/C_x=0.72, y/C_x=0.025) from $t/T = 0.48$ to 0.56. Peak turbulence in the separated shear layer reaches a maximum of $31\%U_{in}$ during this period, which convects downstream along the separated shear layer from (x/C_x=0.8, y/C_x=0.05) at $t/T = 0.56$ to (x/C_x=0.84, y/C_x=0.08) at $t/T = 0.65$.

A localized increase in Δu_{mean} is evident beneath the shear layer at (x/C_x=0.81, y/C_x=0.02) due to elevated turbulence at $t/T = 0.56$. This region quickly loses continuity with the shear layer and convects downstream alone. Once the wake has completely passed, a very slight "calming effect" is evident in depressed u_{rms} levels from $0.80 < t/T < 1$. At $t/T = 0.02$ the u_{rms} levels recover their pre-wake levels and remain there until the next wake passing.

During the interval between wakes, the shear layer in Fig. 13 does not migrate upstream to the steady state location shown in Figs. 7 and 9. Time-space plots of u_{mean}/U_{in}, u_{rms}/U_{in}, and intermittency at a wall normal distance within the shear layer ($y/C_x = 0.049$) are displayed in Fig. 15a to further illustrate this phenomena. At $y/C_x = 0.049$, the steady state shear layer (no wakes, no VGJs) resides between $0.67 < x/C_x < 0.70$ as indicated by the green highlighted bands on u_{rms} contours in Figs. 15 and 16. Progressing in dimensionless time (normalized by the wake passing period, T=115ms) along the ordinate, the positive velocity perturbation preceding the cylinder wake discussed earlier is distinguished by elevated u_{mean} between $0.4 < t/T < 0.6$. Contours of u_{rms} show the bar wake interacting with the separation zone between $0.5 < t/T < 0.9$. The protracted calm zone that results from the influence of the wake persists for approximately $\Delta t/T = 0.3$. At $y/C_x = 0.049$, the shear layer is always located between $0.78 < x/C_x < 0.88$ (also shown in Fig. 9).

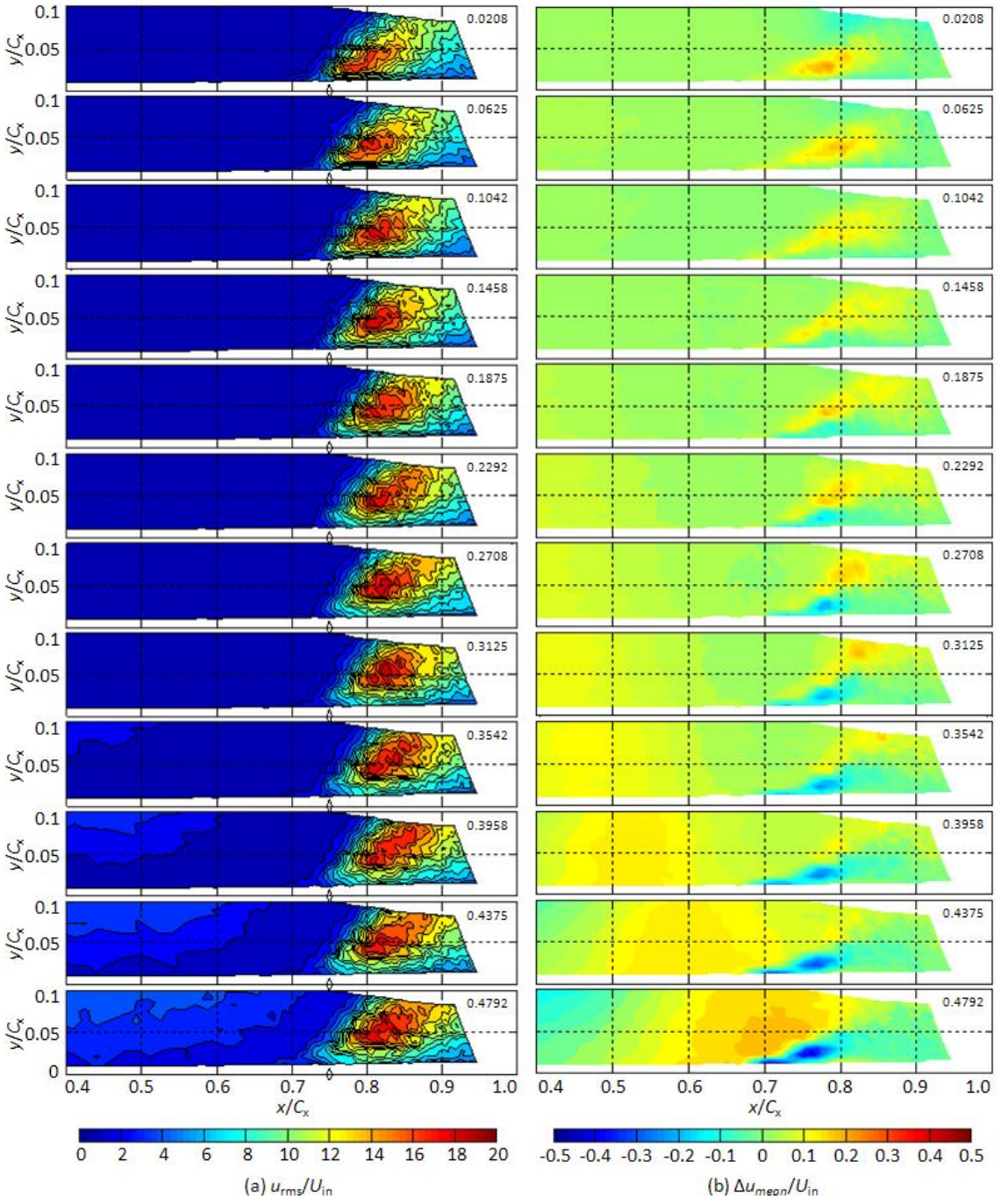

…continued

Figure 13: Time-resolved contours of u_{rms}/U_{in} & $\Delta u_{mean}/U_{in}$ for wakes-only case with F_{red} = 0.41, Re_c =20,000. *Phases 1-12 of 24.*

Figure 13 (continued): Time-resolved contours of u_{rms}/U_{in} & $\Delta u_{mean}/U_{in}$ for wakes-only case with F_{red} = 0.41, Re_c =20,000. *Phases 13-24 of 24.*

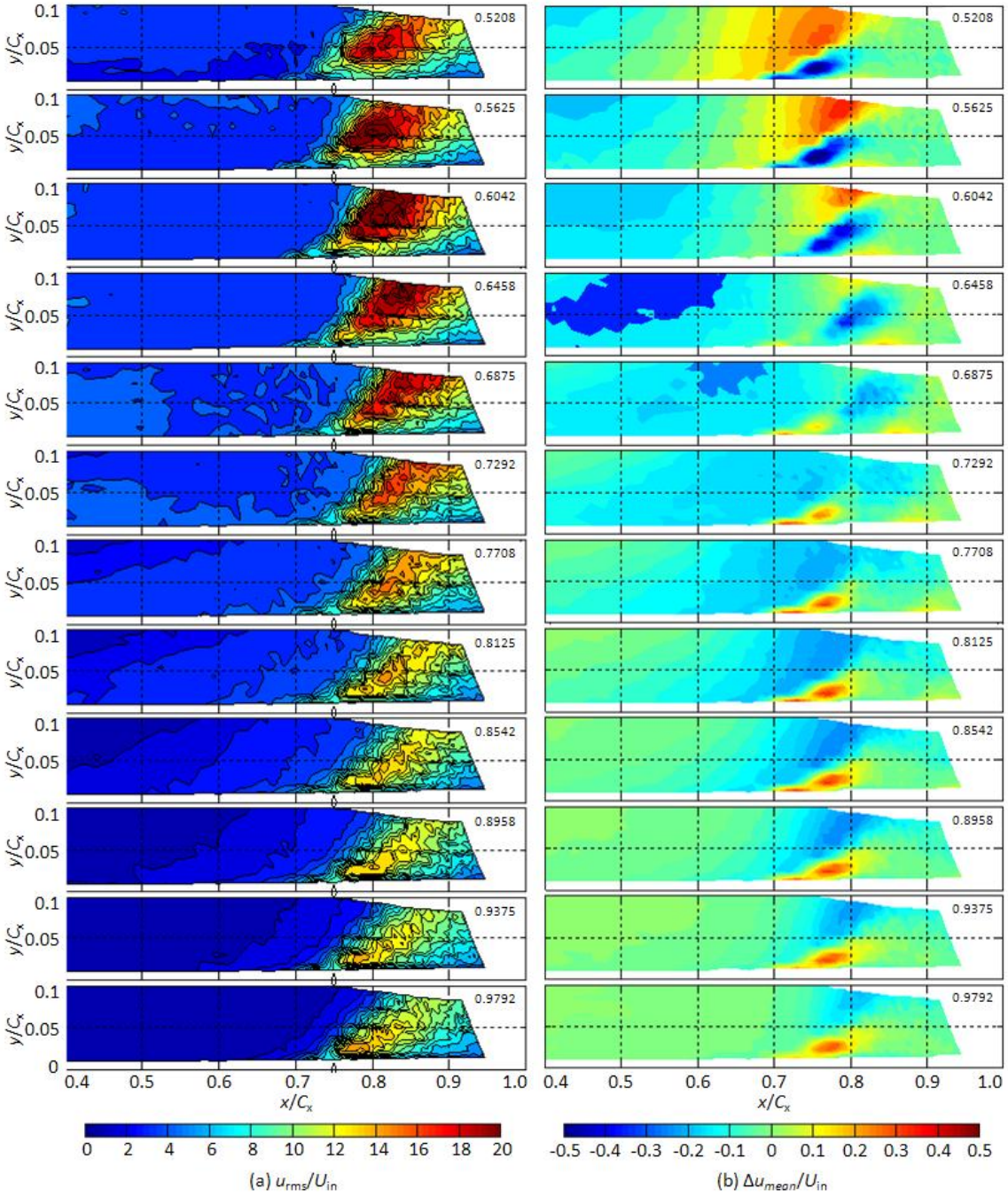

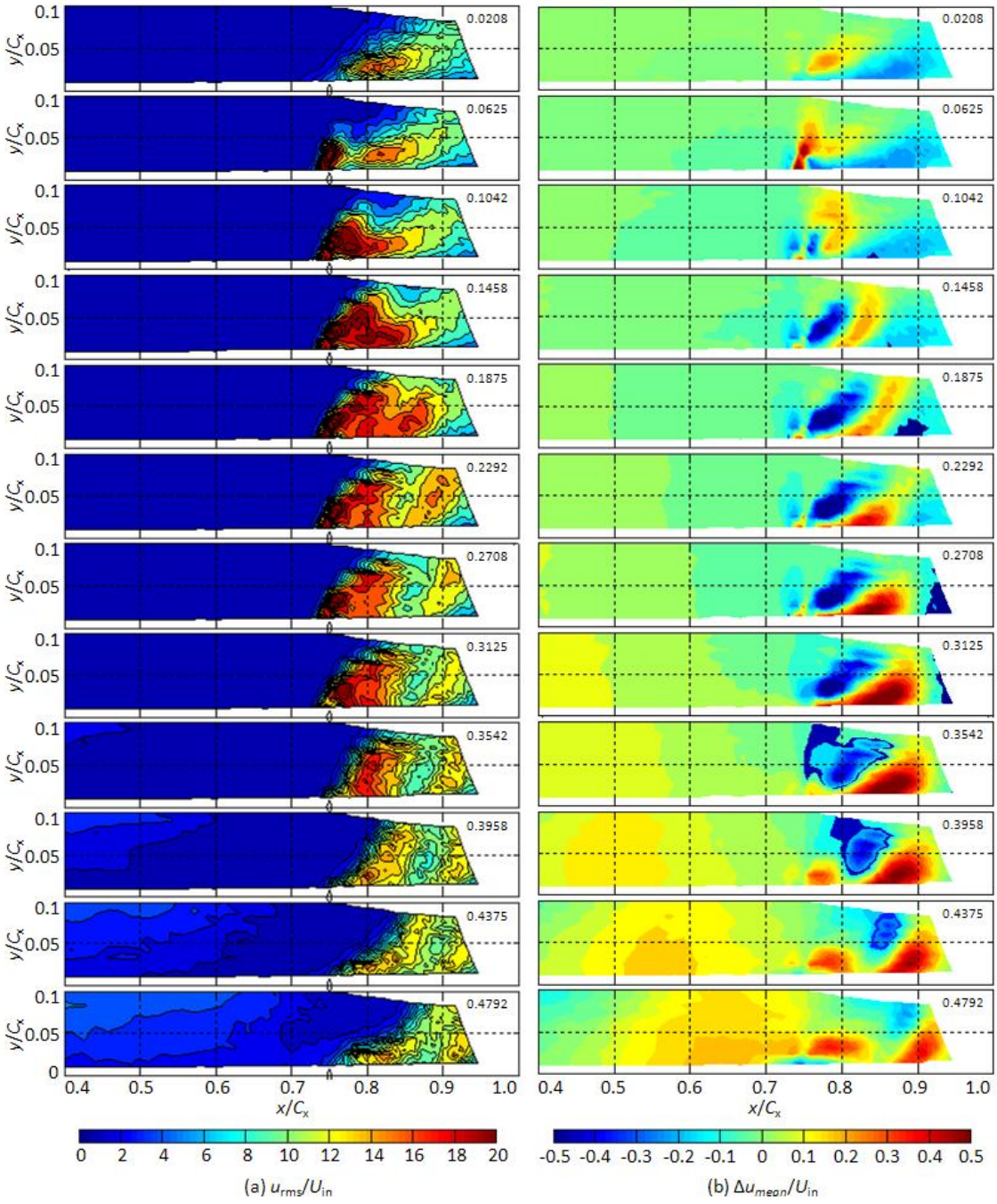

…continued

Figure 14: Time-resolved contours of u_{rms}/U_{in} & $\Delta u_{mean}/U_{in}$ for wakes + DS VGJs with F_{red} = 0.41, Re_c =20,000. *Phases 1-12 of 24.*

Figure 14 (continued): Time-resolved contours of u_{rms}/U_{in} & $\Delta u_{mean}/U_{in}$ for wakes + DS VGJs with F_{red} = 0.41, Re_c =20,000. *Phases 13-24 of 24.*

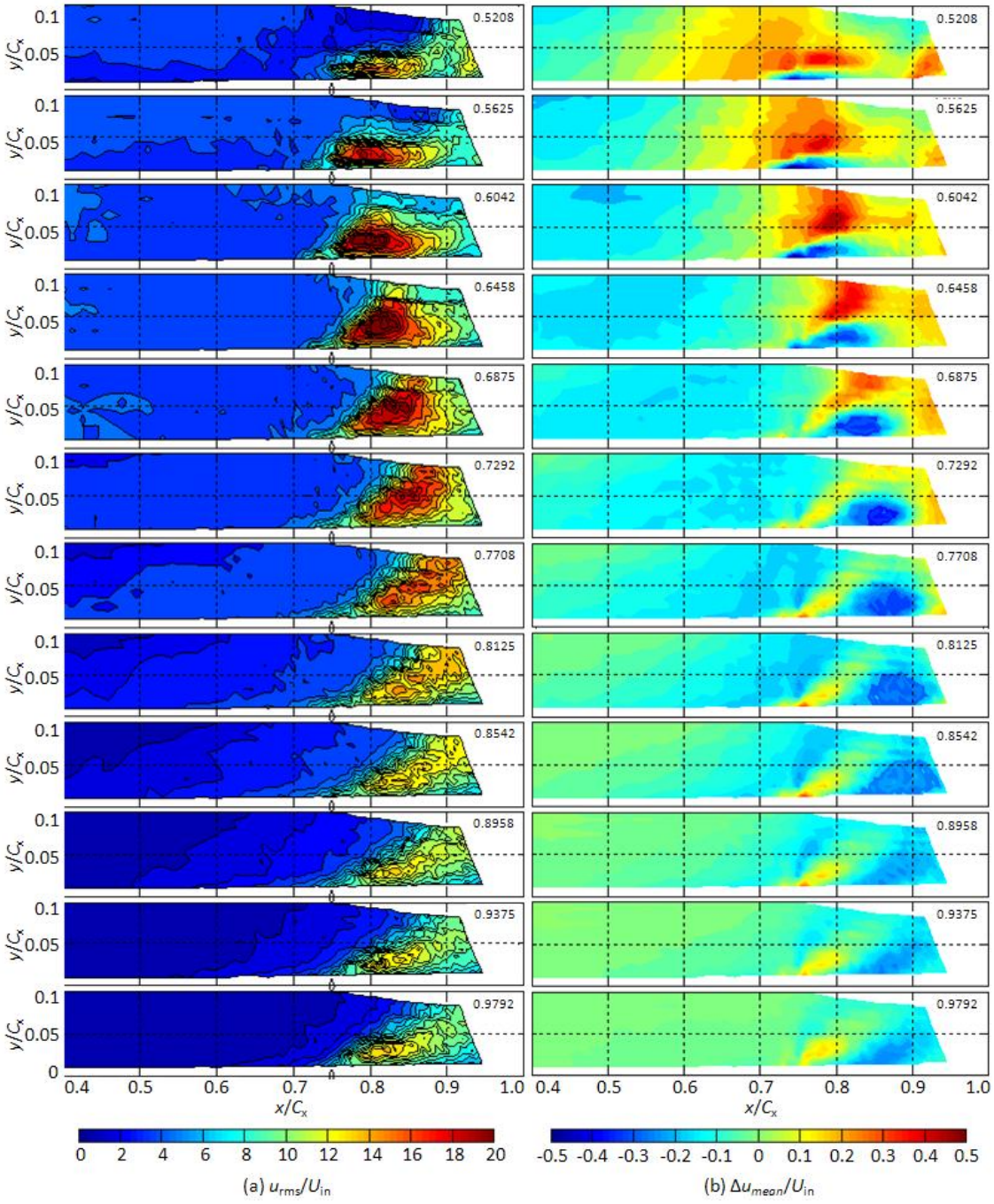

II. Wakes + VGJs at 72%C_x, Fred = 0.41

The combination of wakes + VGJs at 72%C_x results in improved diffusion on the aft portion of the blade that emulates results obtained for the steady state L1A at sufficiently high Reynolds numbers. Aside from the pressure results (Figs. 6 and 10), the time-mean separated shear layer location (Fig. 9) illustrates the impact of adding VGJ flow control to the unsteady wake flow field. While the wake is a spanwise uniform disturbance, having a uniform effect over the entire shear layer (both near-wall and in the far-field), the jets create a near-wall disturbance. Consequently, the jets are most effective at bringing the time averaged shear layer down to the wall.

Figure 15 shows the phase-locked $\Delta u_{mean}/U_{in}$ and u_{rms}/U_{in} data with optimized pulsed VGJ actuation at 72%C_x (actuation occurs at t/T = 0.01, $B_{max} \approx 2$, 25% duty cycle) for 24 discrete phases through the wake passing period. In Fig. 15, the jet effect is evident from $0.06 < t/T < 0.31$ followed by the wake effect from $0.48 < t/T < 0.98$ which is evidenced by elevated u_{rms} fluctuations. The jet is injected downward into the measurement plane which is located 4d below the injection point. Thus, the first evidence of the jet is at t/T = 0.06 and x/C_x=0.75. Throughout the jet pulse the shear layer is observed moving downstream from $0.75 < x/C_x < 0.9$ (Fig. 15a). In Fig. 15b, the jet is responsible for a local deceleration of near-wall fluid indicated by the slight negative perturbation velocity magnitude ($\Delta u_{mean}/U_{in} \approx -0.07$) extending upstream of the jet from x/C_x = 0.75 and relaxing back to zero after the jet is terminated (Fig. 3: t/T = 0.27). Following the pulsed jet disturbance, the boundary layer remains in a controlled state for approximately one convective timescale, evaluated by dividing the suction-side length from the VGJ location to the trailing edge (SSLJ) by the average velocity over SSLJ. The convective timescale for the present application is approximately 0.02 seconds, or one fifth of the forcing period. During this interval ($0.40 < t/T < 0.52$) the boundary layer is thinned with depressed u_{rms} fluctuations, and the separation zone does not migrate upstream to the wake-only mean location. The residual u_{rms} at

t/T = 0.52 is flat against the wall, indicating attached flow transition. This phase lag in the recovery of the separated boundary layer is similar to results reported by Bons et al. [10] for the Pack B.

Before the boundary layer has the opportunity to recover from the jet disturbance, the wake disturbance enters the domain. The wake's positive velocity perturbation is present between $0.31 < t/T < 0.69$ and reaches a peak $\Delta u_{mean}/U_{in}$ magnitude of 0.65 at t/T = 0.60. The perturbation convects through the domain and over a relatively calm, thin boundary layer, still subdued by the VGJ pulse. By t/T = 0.6, u_{rms} levels in the shear layer reach a peak as a result of interaction with the wake disturbance, however the elevated fluctuations are confined to a region that is smaller and nearer to the wall than with wakes alone. Intermittency contours (included in Appendix A) at t/T =0.52 show that transition occurs closest to the surface and the extent of laminar flow above the separation is maximum while the positive velocity perturbation convects over the boundary layer. Figure 15 shows side-by-side time-space plots of u_{mean}/U_{in}, u_{rms}/U_{in}, and intermittency at y/C_x = 0.049 for both wake only and wake + VGJ cases with a wake reduced frequency of 0.41. Indeed, the increased extent of laminar flow over the blade is apparent by comparing intermittency contours with and without VGJs.

Examining the time-space plots, it is easy to see how the jet influences the shear layer differently than the wake. For wakes + VGJs, before the VGJ disturbance the average shear layer position is approximately x/C_x = 0.85 at y/C_x = 0.049, whereas the wake-only average position is x/C_x = 0.80. Comparing time-space contours of u_{rms}, the wake induced calmed zone for the wake + VGJ case exhibits a reduction in turbulent fluctuations (2-3%) from the wake-only case, and lasts twice as long. Between the VGJ and subsequent wake disturbance the shear layer has moved downstream further to nearly 90%C_x. Turbulent fluctuations in the jet induced calm zone [which receives the wake's positive velocity perturbation] are suppressed to a greater extent than in the wake-induced calmed zone.

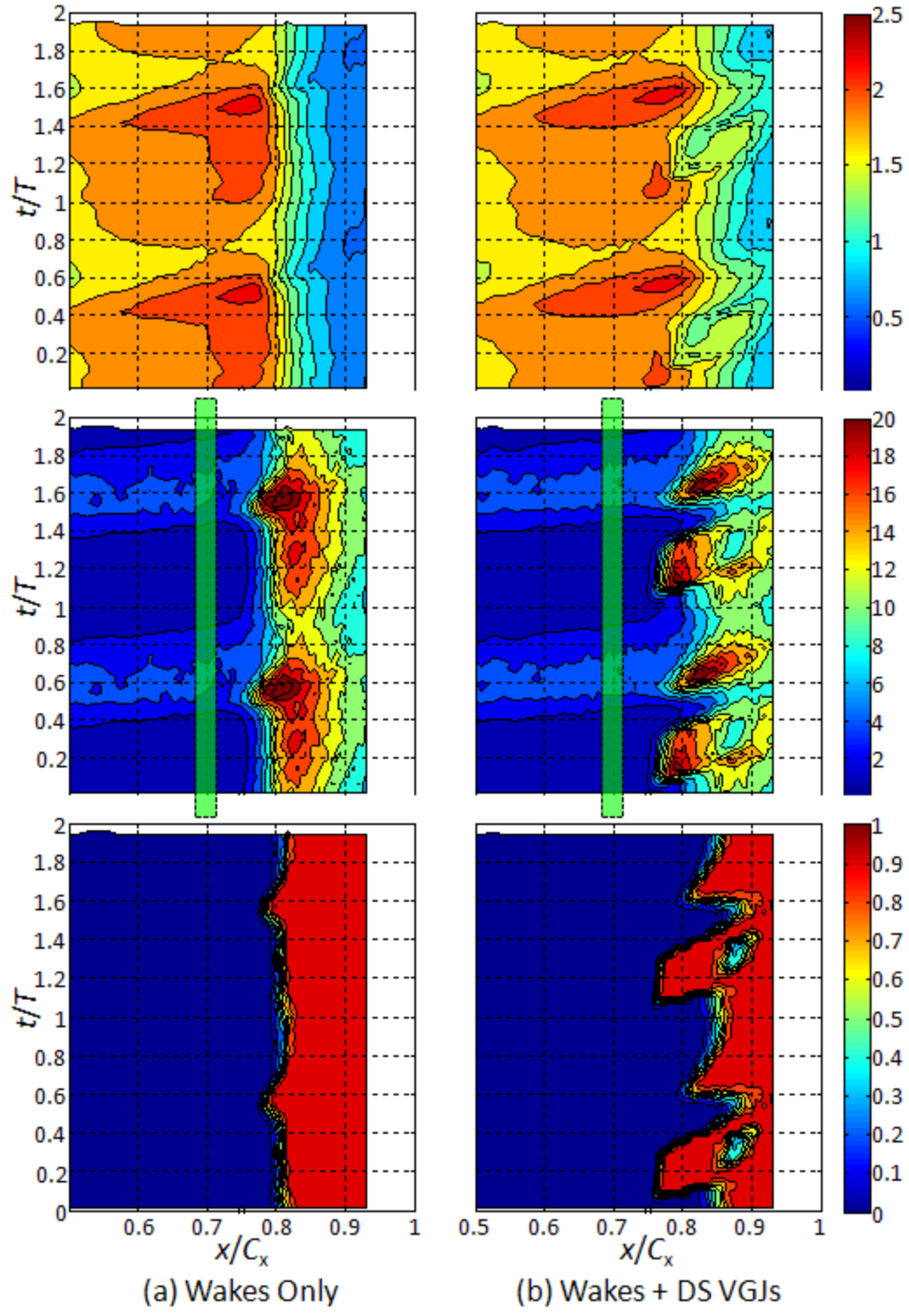

Figure 15: Time-space plots at y/C_x = 0.049 of u_{mean}/U_{in}, u_{rms}/U_{in}, and intermittency for wakes only and wakes + VGJs at 72%C_x. *F_{red} = 0.41,* Re_c *= 20,000. Green highlighted band indicates separated shear layer location for steady state case.*

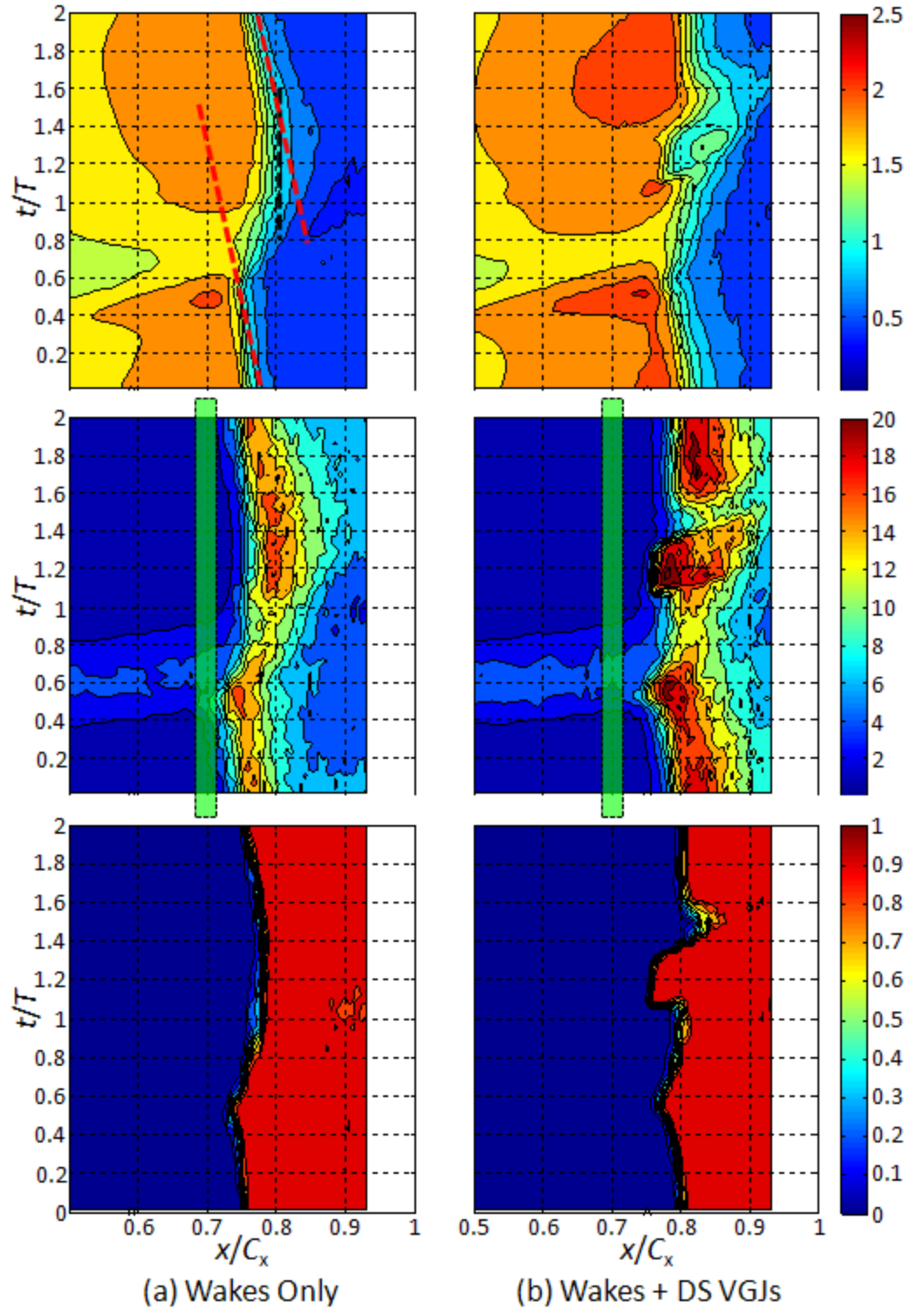

Figure 16: Time-space plots at y/C_x = 0.049 of u_{mean}/U_{in}, u_{rms}/U_{in}, and intermittency for wakes only and wakes + VGJs at 72%C_x (dropped rod). *F_{red} = 0.20,* Re_c *= 20,000. Green highlighted band indicates separated shear layer location for steady state case.*

III. Wakes Only (No VGJs), F_{red} = 0.20

Naturally, it is of interest to determine the time required for the separation zone to recover its wake-only condition following a jet disturbance at 72%C_x in order to better understand the observed synchronization benefit. In order to investigate the phase-lagged boundary layer response to these periodic disturbances, phase-locked hot-film data were acquired with a increased forcing period. Alternate wake generator cylinders were removed, and the flow coefficient was maintained at 0.91, so that F_{red} = 0.20 (F^+ = 0.10). The number appropriately increased number of phases to 48 in order to maintain equivalent temporal resolution. The integrated wake loss for both the wake-only and wake + VGJ cases were double the corresponding values for F_{red} = 0.41 (Fig. 6).

For F_{red} = 0.20 without synchronous VGJ actuation, the characteristics typical of the wake disturbance are present, though the mean shear layer position is shifted approximately 5%C_x upstream from the mean location when the forcing frequency is 0.41 (Fig. 9). As with the presentation of the previous unsteady cases, side-by-side time-space plots of u_{mean}/U_{in}, u_{rms}/U_{in}, and intermittency are presented at the wall normal level, y/C_x = 0.049 in Fig. 16 for unsteady wakes (F_{red} = 0.20) with and without VGJs. (Note: For the cases where F_{red} = 0.20, dimensionless time is normalized by the wake passing period for F_{red} = 0.41, T=115ms, for ease of comparison. Thus, only one forcing cycle is displayed.) Compared to the shear layer response for F_{red} = 0.41, the shear layer orientation changes dramatically through the course of the wake passing period. By examining the contours of u_{rms}/U_{in} in Fig. 16a, it is observed that at y/C_x = 0.049 the shear layer resides between $0.73 < x/C_x < 0.8$ during the interval $0 < t/T < 0.8$. Shear layer unsteadiness is amplified at the beginning of wake interaction, but the magnitude of turbulent fluctuations at y/C_x = 0.049 is roughly 10% lower than when F_{red} = 0.41. The calmed zone persists between $0.8 < t/T < 1$ as before. After the wake convects through the domain ($1.0 < t/T < 1.4$), the shear layer

has moved closer to the blade surface so that its extent at this wall normal level is from $0.78 < x/C_x < 0.87$. A dashed black line with a vertical slope is drawn on the contours of u_{mean} in Fig. 16a to emphasize that the shear layer does not migrate upstream during this interval. After $t/T = 1.4$, the shear layer migrates upstream, at an approximately constant speed, indicated by a dashed red line. Thus the reversion of the separation zone toward its uncontrolled condition appears to be linear until the arrival of the subsequent wake disturbance. Remarkably, even though the shear layer reaches an advanced stage in its recovery between wake events (ie. the shear layer gradually moves upstream between $1.4 < t/T < 0.4$), it still does not return to the steady state location denoted by the green highlighted marker. Since the separation reversion is incomplete, and approximately linear after $t/T = 1.4$, the boundary layer recovery time for this case is estimated by extrapolating the digressing slope of the shear layer motion in the time-space plot. As shown in Fig. 16a, the extrapolation suggests that once the shear layer begins to revert upstream, it may take almost an entire wake-passing period to completely recover its steady state position. Although, this does provide an estimate for the phase-lagged separation recovery, it is significant to note the shortcomings. The mean position of the free shear layer takes on a new equilibrium position for each forcing period. Thus, if the forcing period were reduced to accommodate the recovery time estimated here, the time-mean shear layer position would be different, and so too would be the observed boundary layer reversion. Apparently, the only way to determine the phase-lagged separation recovery time for a given wake reduced frequency is to abruptly end wake generation and tractably resolve the wake migration thereafter, which is outside the scope of this investigation.

IV. Wakes + VGJs at 72%C_x, F_{red} = 0.20

For VGJ actuation at 72%C_x with alternate cylinders removed from the wake generator, the choice was made to retain the same time separation between the wake disturbance and the

following jet pulse. In doing so, the jet-induced "calmed zone" is isolated and the shear layer recovery can be assessed.

For the reduced frequency, F_{red} = 0.20, the addition of pulsed VGJs at 72%C_x, reduces γ_{int} by 46% from the corresponding wakes-only case. As shown in Fig. 9, the time-mean shear layer location is upstream of the VGJs at 72%C_x. Figure 16 shows side-by-side time-space plots of u_{mean}/U_{in}, u_{rms}/U_{in}, and intermittency at y/C_x = 0.049 for unsteady wakes (F_{red} = 0.20) with and without VGJs. At this wall normal distance, the line of peak u_{rms} with flow control always remains between 0.78 < x/C_x < 0.90 (Fig. 16b), whereas with wakes only, the mean position moves forward to 0.73 < x/C_x < 0.84 (Fig. 16a). Moreover, the streamwise extent of the shear layer at y/C_x = 0.049 does not vary as much with VGJs and wakes as it does with wakes only. Comparing the two cases, while the shear layer is still under the beneficial influence of the wake disturbance, the DS VGJs are turned "on" and further suppress the shear layer. At t/T = 1.4, when the shear layer begins to migrate upstream in the wake-only case (Fig. 16a), the u_{rms} data with wakes + VGJs shows a reduction in turbulent fluctuation down to approximately 11% during a brief VGJ-induced calmed zone (Fig. 16b). During the VGJ-induced calmed zone for F_{red} = 0.41, turbulent fluctuation was suppressed to approximately 8%U_{in}. (Fig. 15b). The duration of time for which the shear layer exhibits the "calmed effect" is approximately 13% of the wake passing period for F_{red} = 0.41. The u_{mean} data show that the adjusted shear layer location with VGJ actuation results in greater fluid acceleration over the suction surface immediately after the jet terminates (between 1.4 < t/T < 1.6). Then, at t/T = 1.6, the shear layer abruptly returns to its approximate pre-wake location with a steep rise in u_{rms} up to 27%U_{in}. Corresponding contours of intermittency indicate that while the shear layer is suppressed by jet interaction, the flow attempts to re-laminarize, although this re-laminarization does not endure quite as long as the F_{red} = 0.41 case (Fig. 15b). Recalling that synchronous application with F_{red} = 0.41 was optimized (actuating at t/T = 0, duty cycle = 25%T, $B_{max} \approx 2$), apparently the optimal control parameters are those

which avoid the abrupt shear layer recovery. Furthermore, when aligned, the fluid acceleration resulting from the jet disturbance becomes synergistic with the wake's positive velocity perturbation. In this case, the passage through flow accelerates due to the shear layer recession and reduced flow blockage. The strain applied by the mean flow, which distorts the wake as it convects through the passage, is increased. As a result, accelerated fluid preceding the cylinder wake (ie. the wake's positive perturbation) is sped up. Recall that for F_{red} = 0.41, peak values of the wake's positive perturbation magnitude were 0.35 (t/T = 0.56) without VGJs and 0.65 (t/T = 0.6) with VGJs. The strength of the perturbation is nearly doubled by alignment with the jet-induced calmed zone, and it persists longer. In turn, the wake precursor may be providing additional streamwise momentum to the near-wall flow, thereby further suppressing the shear layer. When appropriately combined, the synergistic benefits of the wake's positive perturbation and the jet-induced calmed zone exceed those afforded otherwise.

3.2.3. γ_{int} Analysis of VGJ Blowing Ratio and Chordwise Location

As shown in Fig. 6, pulsed VGJ actuation at 59%C_x dominates the flow field, regardless of whether periodic wakes are present. Meanwhile, the impact of VGJs at 72%C_x is muted when the downstream jets are well into the separation zone. It is significant that control is still effective deep into the separation zone, but this reduced effectiveness of the downstream VGJs indicates that this chordwise location represents a threshold where jet penetration is obstructed and controllability may be limited.

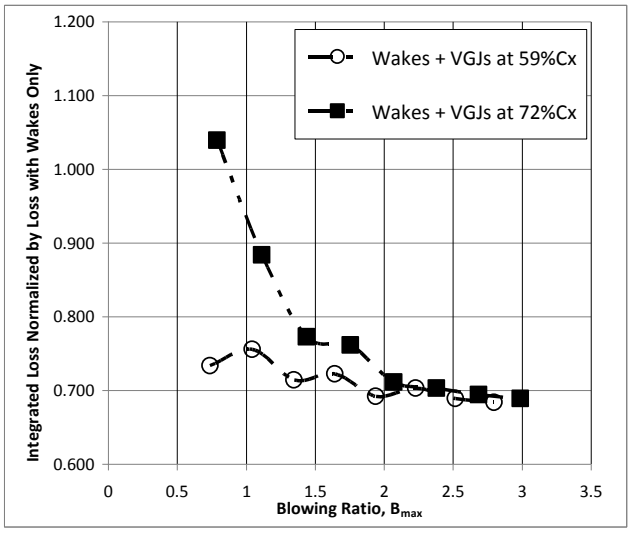

Figure 17: Wake total pressure loss normalized by loss with wakes only plotted against blowing ratio. *Data for VGJ actuation at 59% and 72%C_x on the suction surface of the L1A, optimally synchronized with simulated unsteady wakes, F_{red} = 0.41,* Re_c *= 20,000.*

To further illustrate this shortcoming, Fig. 17 shows the results of a blowing ratio study, based on γ_{int} normalized by the value for wakes only (F_{red} = 0.41), conducted with synchronous actuation between wake events at the appropriate phases in the wake passing period. The flow coefficient and wake reduced frequency were maintained at 0.91 and 0.41 respectively. The feed pressure was varied by increments of 10psi for each row of jets, and the jet exit velocity is known via hot-film data acquired while injecting into quiescent surroundings. While actuating at either axial position provides comparable benefits for $B_{max} > 2$, actuation at 72%C_x is less effective for $B_{max} < 1.5$. Moreover, for $B_{max} < 0.8$, downstream VGJs represent wasted kinetic energy, increasing the normalized total pressure loss to a value above unity. Evidently the shear layer is too far from the wall to be beneficially influenced by the VGJs at 72%C_x. The downstream jets require a minimal B_{max} setting in order to penetrate through the region of separated fluid and succeed in mixing high-momentum freestream fluid with the low-momentum near wall fluid. Conversely, the upstream jets offer robust control and exhibit little sensitivity to either phase synchronization or the blowing ratio control parameter.

There are two mechanisms by which VGJs affect separation. The disturbance alone can trigger transition, as is the case when actuating near the suction peak. Second, VGJs generate a counter-rotating pair of streamwise vortices, of which one leg decays. The remaining vortex leg convects over the surface, penetrating the separated region and entraining high-momentum fluid from the freestream toward the bounding surface. This study provides insight into the role of these mechanisms, and how they combine to modify the separation boundary layer of the L1A. Since the upstream VGJs are effective for relatively low jet strength, it is concluded that perturbing the flow near the suction peak is sufficient to trigger transition. The downstream VGJs are effective for a sufficiently high blowing ratio. On the other hand, the downstream jets are actuated at the threshold of the separation, just after the separated layer has under wake-induced bypass transition. Furthermore, velocity profiles in the "calmed zone" have a full, turbulent shape. Consequently, small disturbances ($B_{max} < 1.5$) buried within the layer (VGJs at 72%C_x) are likely broken down by small-scale turbulence. This suggests that at the downstream location, streamwise vorticity may be the prevailing mechanism by which VGJs influence the separation.

3.2.4. Two-Dimensional Phase-Locked PIV Data

The phase-locked PIV data, collected at the spanwise level 4*d* below the top of a midspan VGJ, are presented in the following order. First the *wake-only* case ($F_{red} = 0.41$) is presented and the notion of the negative jet is discussed. Then data for the case including optimal synchronous VGJ actuation with wakes ($F_{red} = 0.41$) is presented. Of the 24 phases recorded for each dataset, illustrative phases throughout the wake passing period are presented in the interest of saving space (unless otherwise noted). At each of these phases, several quantities are used to describe the ensemble-averaged flow field. Contour plots of velocity magnitude, fluctuating velocity, and swirl strength along with vector plots of both total and perturbation velocity vectors are presented. Note that the data is presented in the dimensional PIV camera coordinate system.

In complicated flow fields, large-scale structures may be concealed by regions of substantial shear stress, making it difficult to identify these structures and determine their

contribution to the flow field. The swirl strength (*Sw*) is used here to unveil spanwise vortical structures [42-44]. The swirl strength is defined at the positive imaginary part of the eigenvalues of the ensemble-averaged velocity gradient tensor at each point in the measurement domain. It is calculated with length and velocity normalized by axial chord and inlet velocity, respectively. The camera coordinates are used, so that the *x* coordinate is positive in the approximate downstream direction.

Similar to the calculation of perturbation velocity magnitude (Δu_{mean}) performed with the hot-film data, the calculation of perturbation velocity vectors at each point in the measurement domain is accomplished by taking the cycle-average of each *u* and *v* velocity components (averaging all 24 phases), and then subtracting the time-mean quantities from the phase-locked ensemble-averaged *u* and *v* components.

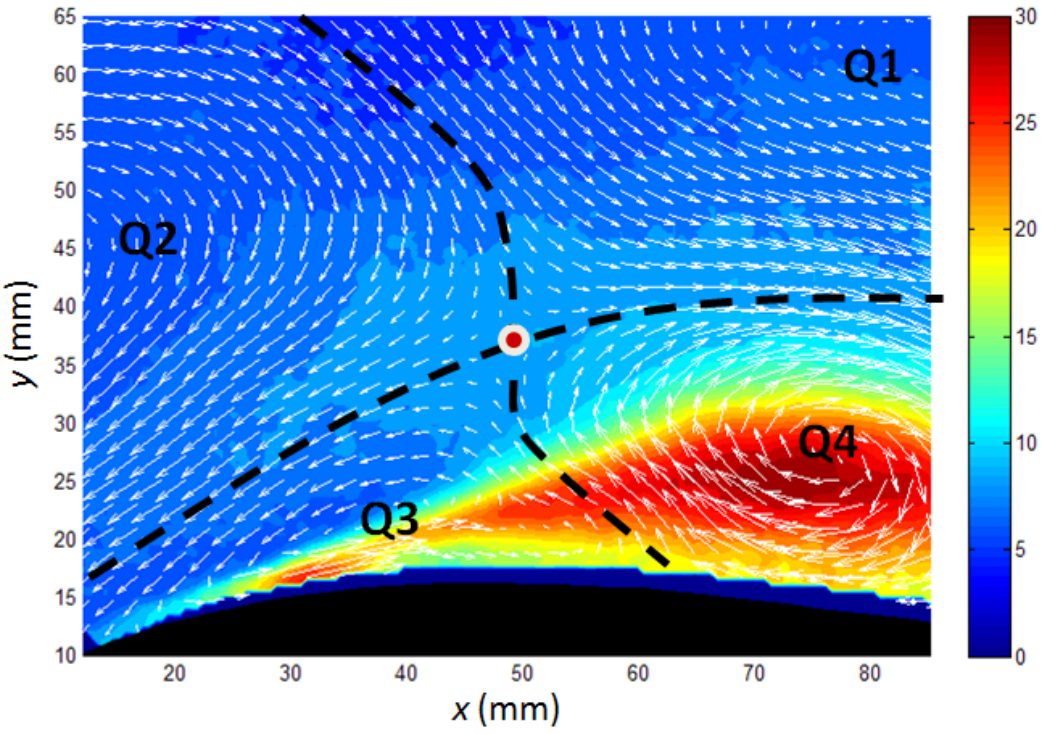

Figure 18: Sample figure from wakes-only case (F_{red} = 0.41), contours of fluctuating velocity magnitude superposed with perturbation velocity vectors. *Showing the existence of a vortical quadrupole structure whose saddle point is near the intersection of the black dashed lines. The naming convention is indicated by the symbols at the eye of each vortex.*

To aid in the description of the structures that exist in the data presented herein, an adopted naming convention is first introduced. Figure 18 is a sample figure showing contours of fluctuating velocity magnitude superposed with perturbation velocity vectors from the wake-only case at $t/T = 0.6042$. The region of highest fluctuating velocity ($U_{rms} > 20\%U_{in}$) is the suction side boundary layer, and the region where $U_{rms} \approx 10\%U_{in}$ is the wake disturbance which enters the domain from the upstream boundary (left). At this measurement phase, the wake's negative jet is clearly impinging on the separated region. Careful inspection of the perturbation velocity vectors in this figure show the existence of a spanwise-vortical quadrupole structure. Dashed white lines approximately divide the structure into quadrants, and the intersection of the two white lines is near the saddle point of the quadrupole which is convecting above the free shear layer. Each of the four vortices is designated Q1, Q2, Q3, or Q4 (as shown in the eye of each vortex) according to which quadrant the vortex belongs.

The two-dimensional PIV data for the wake-only case is presented in Figs. 19 through 22. Unless otherwise noted, each figure includes ensemble-averaged results for 8 of 24 measurement phases equally space in time through the wake passing period. Figure 19 displays wall-normal velocity profiles at four streamwise stations equally spaced along the suction side length in the measurement domain. Figure 20 displays the corresponding contours plots of U_{rms} magnitude superposed with the perturbation velocity vector field (ΔU_{mean}). Figure 21 shows contours of U_{mean} magnitude, which is followed by contours of swirl strength (Sw) in Fig. 22. For this case (wakes-only), swirl strength is presented for all 24 measurement phases convey the existence of coherent structures evidenced in the ensemble-averaged data. The PIV results acquired for the case with wakes and VGJs at $72\%C_x$ are presented in Figs. 23-26 in the same order and format as Figs. 19-22.

I. L1A with Unsteady Wakes Only (No VGJs), F_{red} = 0.41

Prior to the interaction of the wake and separated shear layer, between $0.02 < t/T < 0.27$, the shear layer resides in the time-mean location, evidenced by the negligible magnitude of the perturbation velocity vectors throughout the flow field (Fig. 20). Instantaneous images showing evidence of vorticity shedding during this interval are presented in Appendix B. The contour plots of swirl strength in Fig. 22 include all 24 measurement phases in order to show that during certain intervals, vortex shedding does seem to lock in to the wake forcing. Between $0.15 < t/T < 0.40$, preceding the wake disturbance, dense regions of elevated *Sw* are observed convecting over the suction surface. Recalling that these contour plots are the ensemble-average of 800 PIV image sets, it is remarkable that this alignment is visible in the ensemble-averaged data. The alignment of coherent vortex shedding six measurement phases (starting at $t/T = 0.10$) prior to the wake's arrival ($t/T = 0.40$) in the measurement domain suggests that perhaps the influence of the wake disturbance is communicated via a potential field. The trajectory of these coherent structures is also indicated by red lines which pass through several of the dense regions. The slope of red lines drawn across these first six measurement phases, suggests that these structures are convecting over the suction surface at half of the local boundary layer edge velocity ($0.5U_e$). This assertion is corroborated by identifying the vortex convection velocity magnitude in Fig. 21. In general, the convective velocity of a vortex is the velocity at the vortex center. For example, examining Fig. 22, at $t/T = 0.27$, a vortex is centered at approximately (x,y) = (58mm, 24mm). At $t/T = 0.31$, the vortex center appears to have shifted to (x,y) = (48mm, 22mm). Normalized by the inlet velocity, the vortex convective velocity is estimated to be $U_{con}/U_{in} \approx 1$. In Fig. 21, at $t/T = 0.27$, the normalized velocity magnitude at (x,y) = (58mm, 24mm) is $U_{mean}/U_{in} \approx 1.1$. The normalized local edge velocity (U_e/U_{in}) is 2.1. It is also noted that the structures are strongest where they originate, and within one to two wavelengths downstream of their inception, these large-scale structures are

broken down into less organized, small-scale structures. This suggests that prior to the wake disturbance this vortex shedding mode may be the driver for transition to turbulence, as these large-scale structures transfer energy from the mean flow to smaller scales.

The wake is clearly present at the upstream boundary of the domain at t/T = 0.40, evidenced by elevated levels of velocity fluctuation. Preceding the wake, contours of U_{mean}/U_{in} (Fig. 21) show an increase from 2.1 at t/T = 0.27 to a cycle maximum of 2.4 at t/T = 0.52. The corresponding plots of the perturbation velocity field (Fig. 20) also show a substantial positive streamwise perturbation above the cycle mean which convects over the shear layer. Upon careful inspection, this perturbation appears as the lower portion the Q1 vortex. During the same interval, contours of U_{rms} indicate intensification of the free shear layer instability. The shape of the velocity profile downstream of the shear layer turbulent breakdown becomes slightly more inflectional. This is especially evident in the second and third velocity profiles (counted from left to right) at (x, y) = (35mm, 17mm) and (x, y) = (50mm, 17mm), progressing from $0.27 < t/T < 0.52$. By t/T = 0.52, the wake impinges on the separated region completely. The boundary layer thickness increases in the wall-normal direction while evidently contracting in the streamwise direction and shifting further downstream (Fig. 21). Between $0.40 < t/T < 0.52$, The peak level of U_{rms} is displaced downstream from $x \approx$ 57mm to $x \approx$ 62mm. A structure is visible (Q4) in contours of U_{mean}/U_{in} (Fig. 21). Above the shear layer at the location of peak unsteadiness is the aforementioned positive streamwise perturbation. At the same location beneath the edge of the shear layer, is a pocket of reverse flow attaining levels as high as 25% of the edge velocity at t/T = 0.52. The structure is most easily observed by vectors of the perturbation velocity field. The aforementioned positive perturbation increases inflection of the local velocity profile which can be seen in Fig. 19 at (x, y) = (65mm, 17mm) between $0.40 < t/T < 0.65$. The positive streamwise perturbation effectively enhances wall-bound vorticity and initiates the rollup of vorticity embedded in the boundary layer into the Q4 vortex. This rollup is clearly shown in the

measurement domain between $0.52 < t/T < 0.65$ by the clockwise vortex whose core coincides with the peak unsteadiness and the increased boundary layer thickness. Examining the perturbation velocity field (Fig. 20), another clockwise vortex (Q2) is observed entering the domain at $t/T = 0.52$. This is the image of the wake's *negative jet* bifurcating into two streams as the jet impinges on the suction surface. Peak unsteadiness in the wake occurs at the point where the two streams divide. It is worthy to note the negative jet's inability to penetrate the separated shear layer. The interaction of the wake and free shear layer is thus characterized by the existence of a quadrupole structure whose saddle point convects over the shear layer, rather than along the blade surface.

Between $0.52 < t/T < 0.64$, the point of peak unsteadiness (Fig. 20) at the core of Q4 convects downstream under the influence of the freestream and increases to a maximum value of $35\%U_{in}$. Examining Fig. 22, Q4 appears as a very strong vortex travelling at approximately 50% of the boundary layer edge velocity as indicated by the dashed red line which intersects Q4 at each measurement phase. As before, the eye of Q4 is identified near (x,y) = (64mm, 25mm) at $t/T = 0.52$. Referring to Fig. 21, the convective velocity of Q4 is $U_{con}/U_{in} \approx 1.2$ and the local edge velocity is $U_e/U_{mean} \approx 2.4$, thus $U_{con} \approx 50\%U_e$. The boundary layer fluid response lags the freestream, and between $0.52 < t/T < 0.65$, Q1 actually begins to overtake Q4. Simultaneously, Q4 comes under the influence of the Q2, which can be observed interacting with the separated region in Fig. 20 at between $0.65 < t/T < 0.90$. During this interval, the negative jet fluid nearest the wall, belonging to Q2, points upstream. This negative streamwise perturbation convects above the free shear layer reducing the inflectional quality of the local surface normal velocity profile as shown in Fig. 19. Specifically, the second, third, and fourth profiles (counted from left to right) exhibit no reverse flow near the blade surface. Consequently, the boundary layer rollup structure (Q4) begins to weaken, evidenced by a lower edge velocity and decreasing unsteadiness between $0.52 < t/T < 0.65$. As Q2 interacts with the separation zone, the fluctuating velocity component

(U_{rms}) decreases from levels between 25-35%U_{in} before interaction with Q2, to levels between 15-25%U_{in} at t/T = 0.90. This is the well documented "calmed zone" which ensues after the wake disturbance. This negative streamwise perturbation can also be seen in contours of U_{mean}/U_{in} (Fig. 21) as a region of low speed convecting over the free shear layer. Because the free shear layer and extensive separation prevent penetration of wake structure toward blade surface, the formation of fluid structures in the boundary layer play an important role. Upon careful inspection of perturbation velocity vectors between $0.52 < t/T < 0.65$, generation of a second vortex within the boundary layer (Q3 having a counter-clockwise sense) is observed, illuminating a saddle point in the approximate center of a skewed quadrupole vortical structure which is convecting just above the free shear layer. Given its sense (clockwise), fluid upstream of Q4 is kicked away from the surface by the ejecting motion of Q4. The sense of Q3 (counterclockwise) is a result of the influence of Q4 and Q2. As the quadrupole translates over the aft portion of the suction surface, it alternates the velocity profile shape between inflectional and full.

Looking again to the contours of *Sw* in Fig. 22, between $0.69 < t/T < 0.94$ regions of swirl strength are still observed, although they are weaker and more difficult to discern. The existence of these rollup structures in the ensemble-averaged data suggests that the receptivity of the free shear layer to disturbances encourages vortex rollup and shedding to align with the wake forcing throughout the wake-passing period.

At t/T = 0.77, the negative streamwise perturbation which was previously covering the free shear layer exits the domain, although a rise in U_{rms} lags Q2 by several measurement phases. Between $0.90 < t/T < 0.02$, the separation begins to revert back to its unperturbed condition under the influence of the strong adverse pressure gradient. As the wake disturbance completely exits the domain, fluid accelerates over the suction surface as observed in Fig. 21 by an elevated magnitude of U_{mean}/U_{in} from $0.89 < t/T < 0.40$, when the subsequent wake enters the domain.

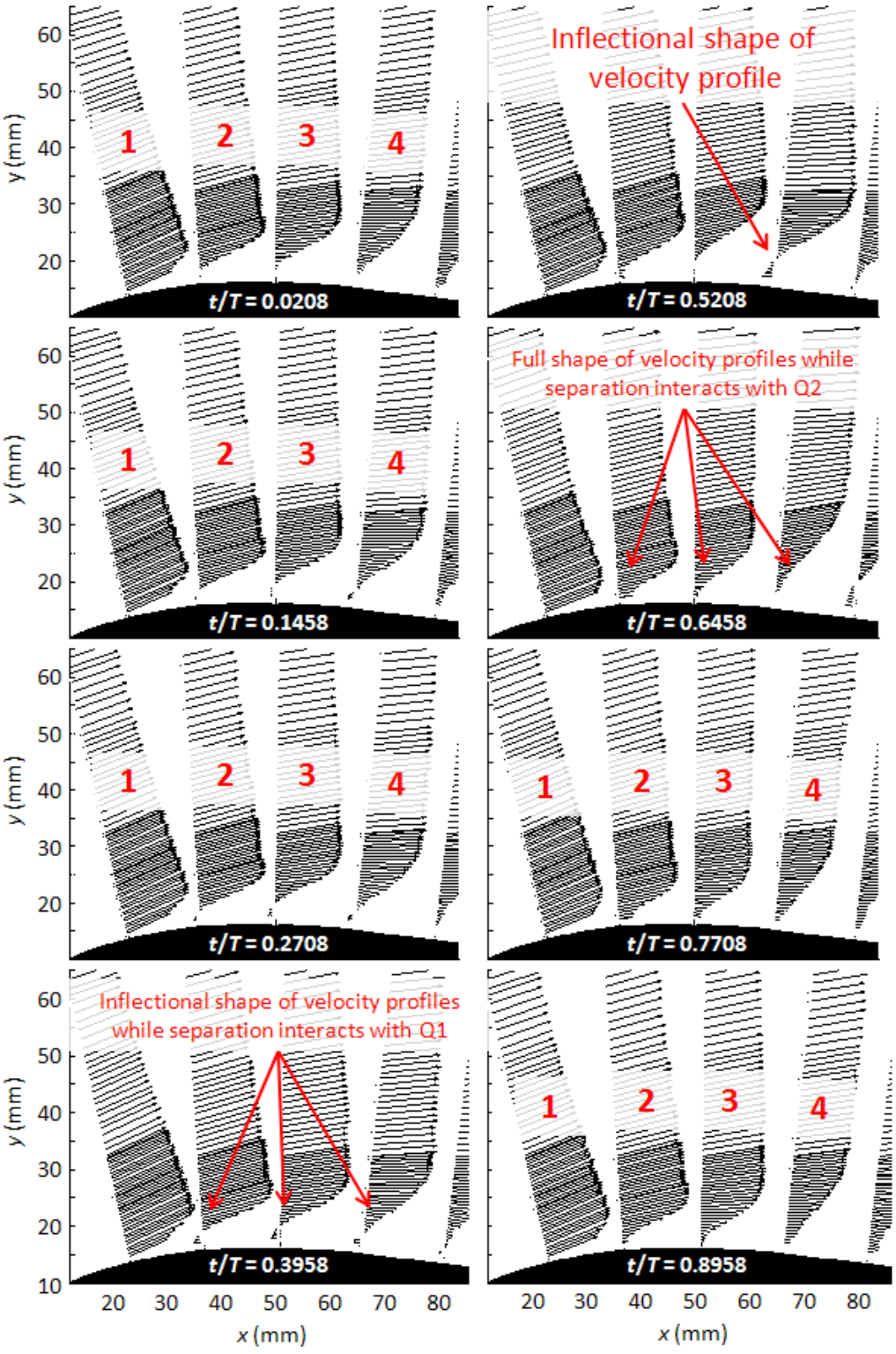

s

Figure 19: Ensemble-averaged streamwise velocity profiles for wakes-only (F_{red} = 0.41) at Re_c = 20,000. *Showing 8 of 24 measurement phases {phases 1,4,7,10,13,16,19,22}.*

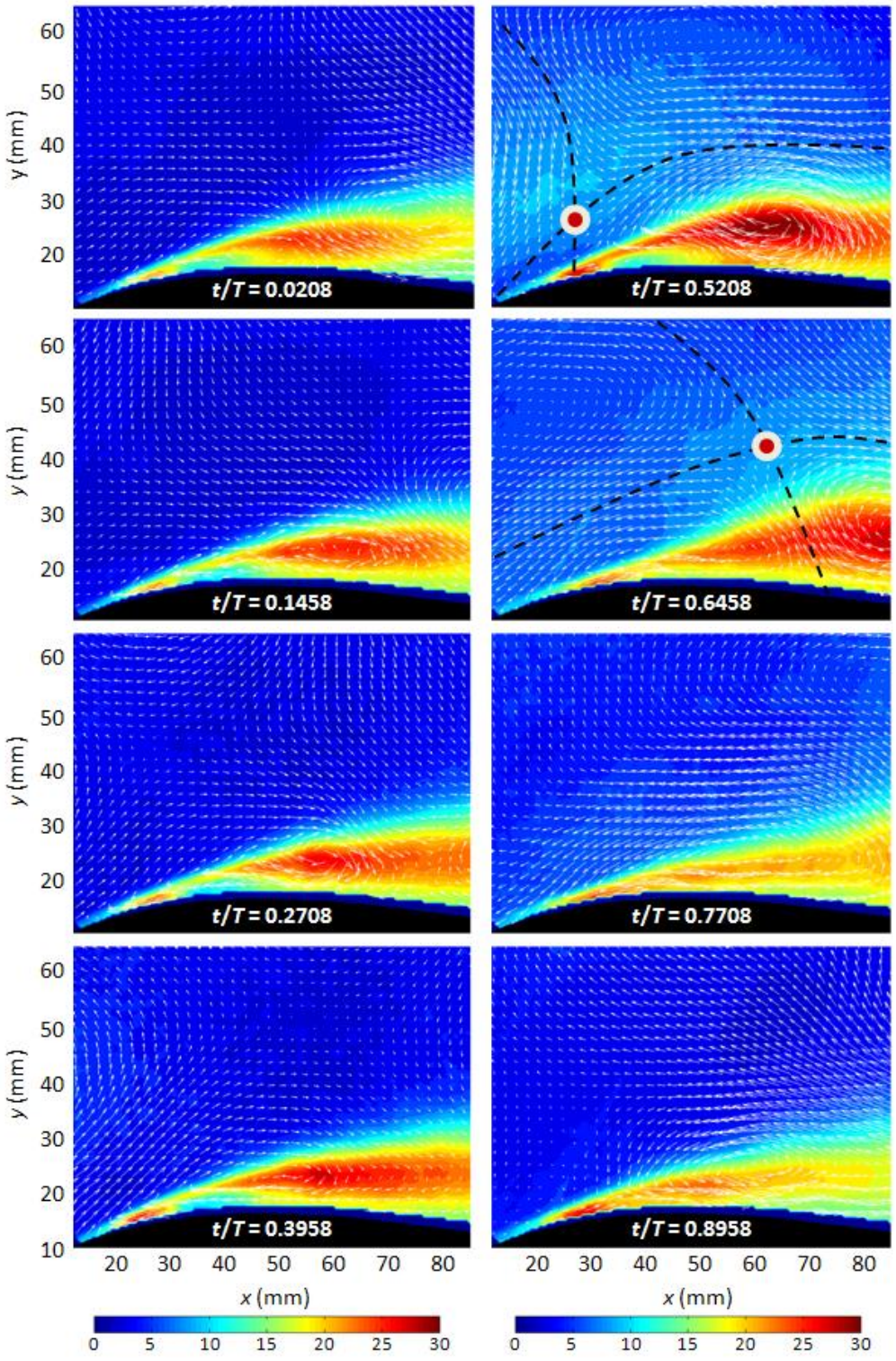

Figure 20: Contours of fluctuating velocity magnitude (U_{rms}/U_{in}) superposed with perturbation velocity vectors ($\Delta U_{mean}/U_{in}$), data for wakes-only (F_{red} = 0.41) at Re_c = 20,000. *Showing 8 of 24 measurement phases {phases 1,4,7,10,13,16,19,22}.*

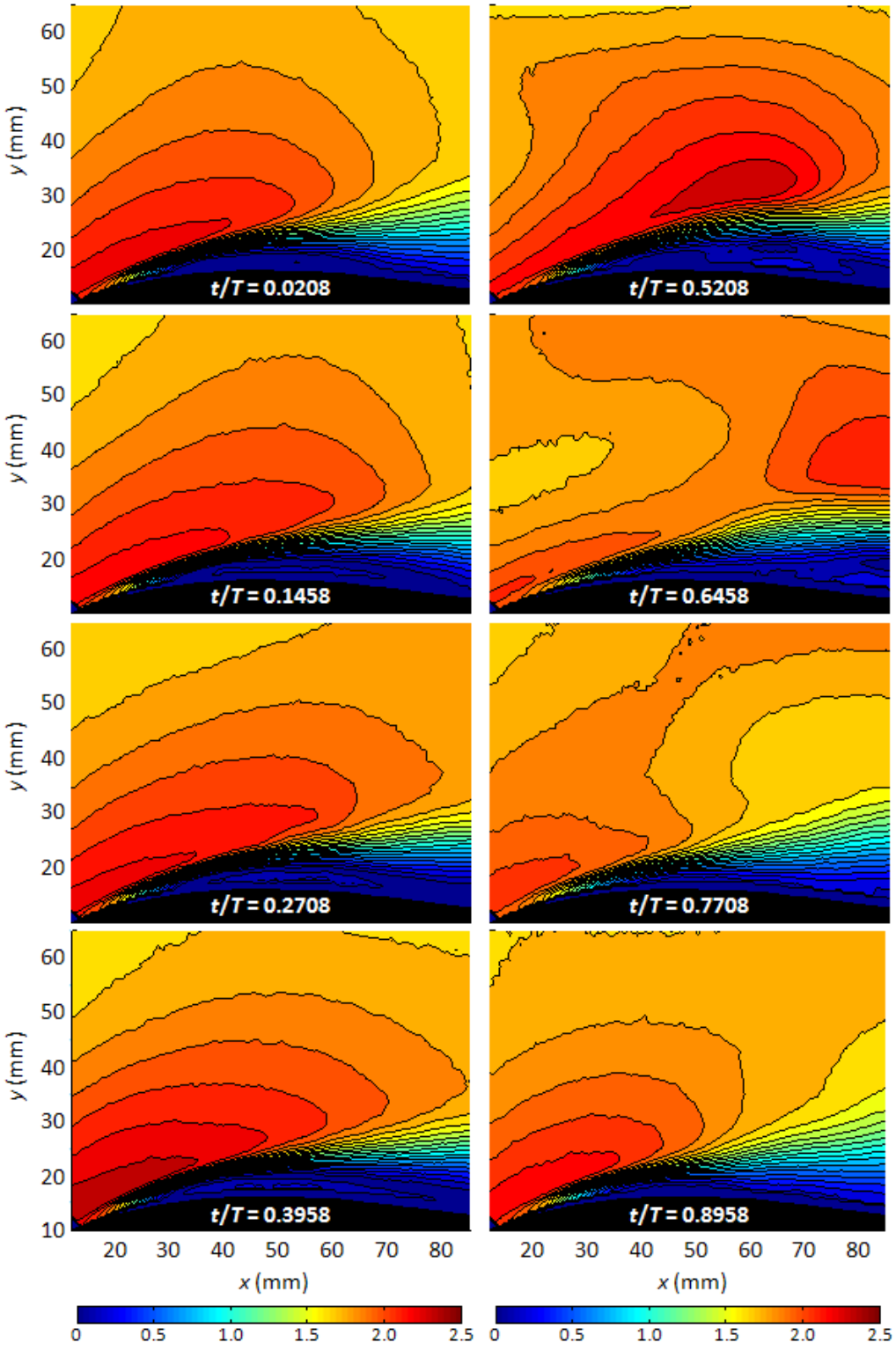

Figure 21: Contours of ensemble-averaged velocity magnitude (U_{mean}/U_{in}), data for wakes-only (F_{red} = 0.41) at Re_c = 20,000. *Showing 8 of 24 measurement phases.*

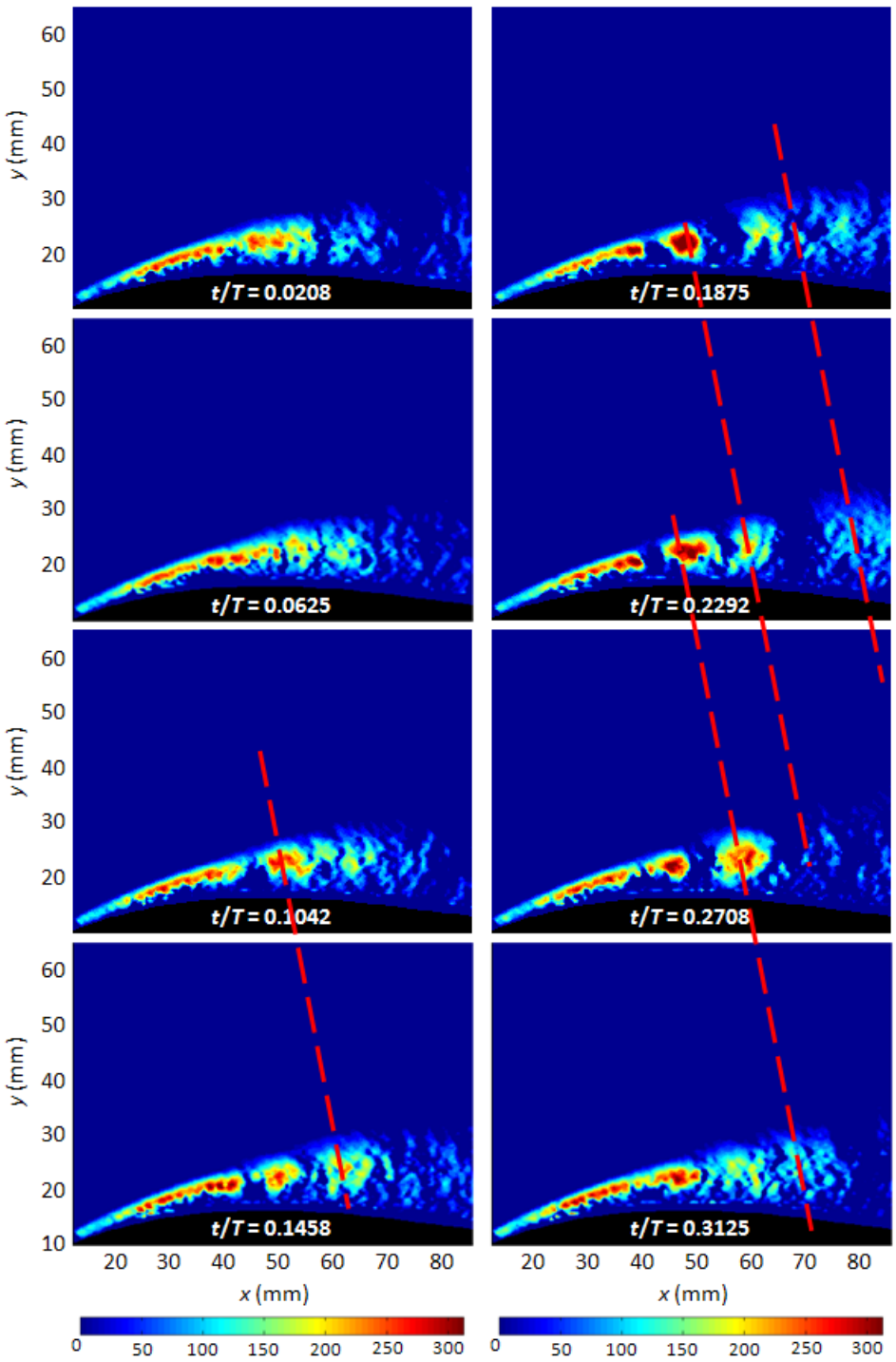

…continued

Figure 22: Contours of ensemble-averaged swirl strength (*Sw*), data for wakes-only (F_{red} = 0.41) at Re_c = 20,000. *Phases1 - 8.*

Figure 22 (continued): Contours of ensemble-averaged swirl strength (*Sw*), data for wakes-only (F_{red} = 0.41) at Re_c = 20,000. *Phases 9 – 16.*

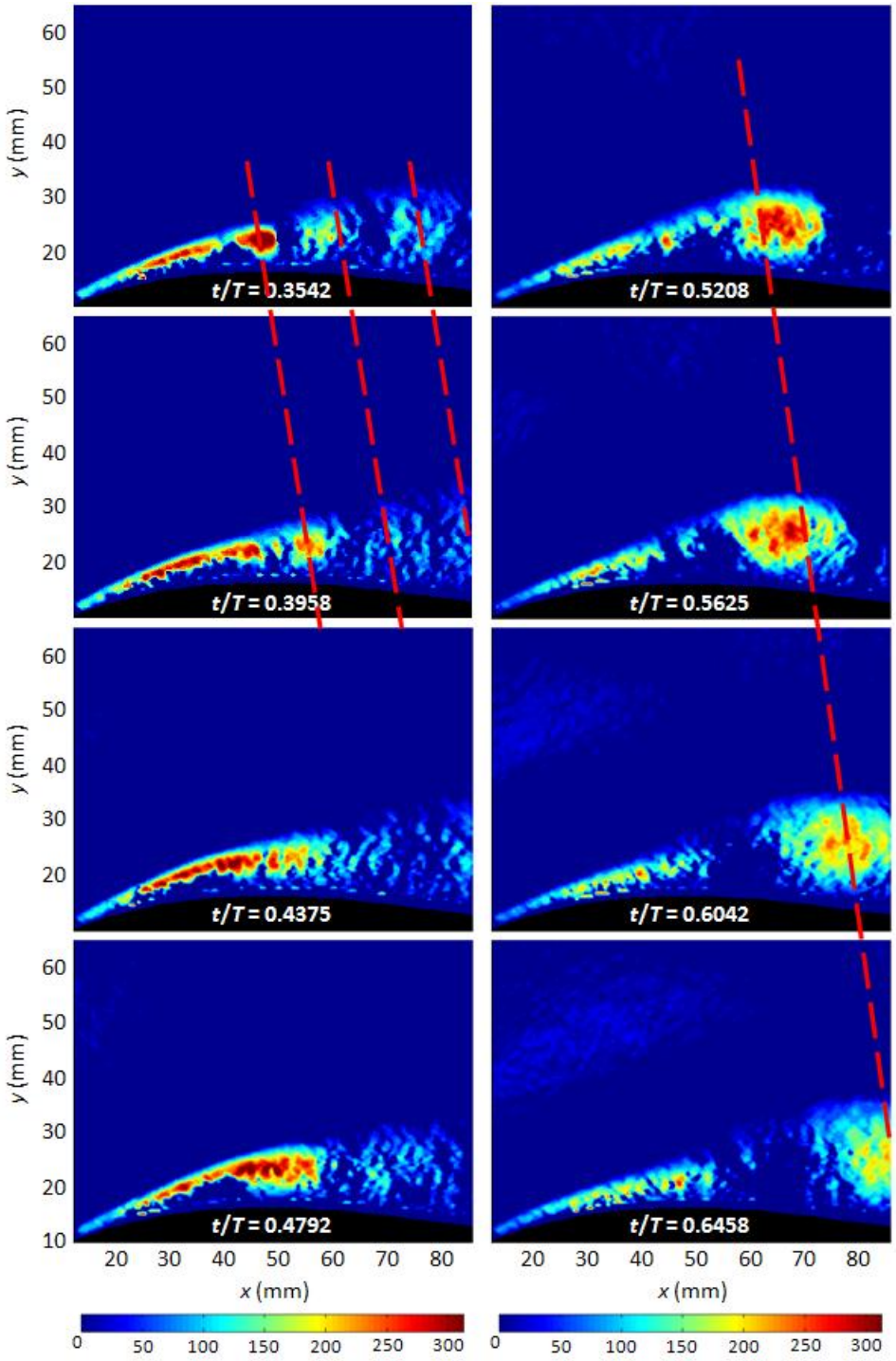

…continued

Figure 22 (continued): Contours of ensemble-averaged swirl strength (*Sw*), data for wakes-only (F_{red} = 0.41) at Re_c = 20,000. *Phases 17 - 24.*

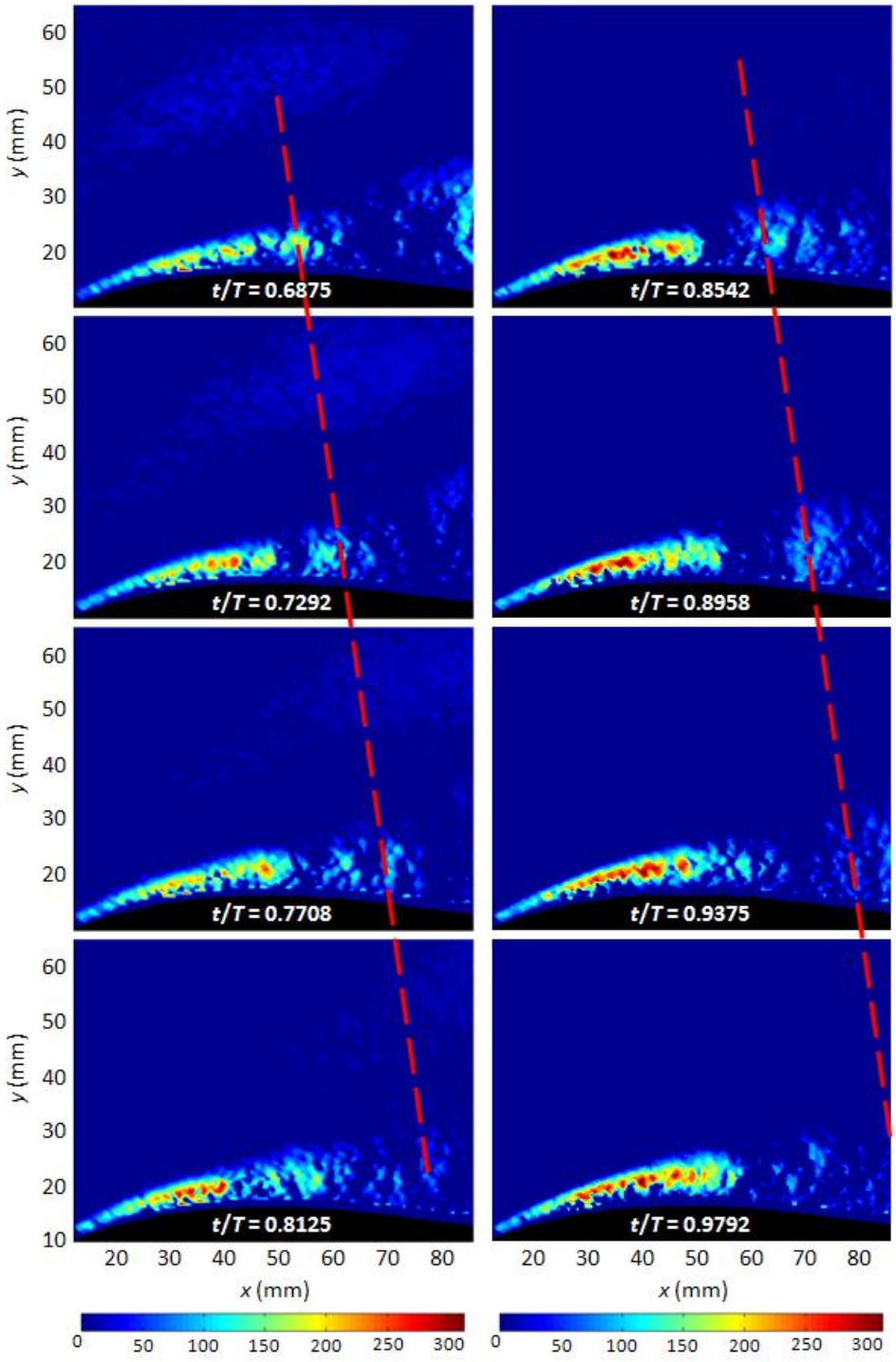

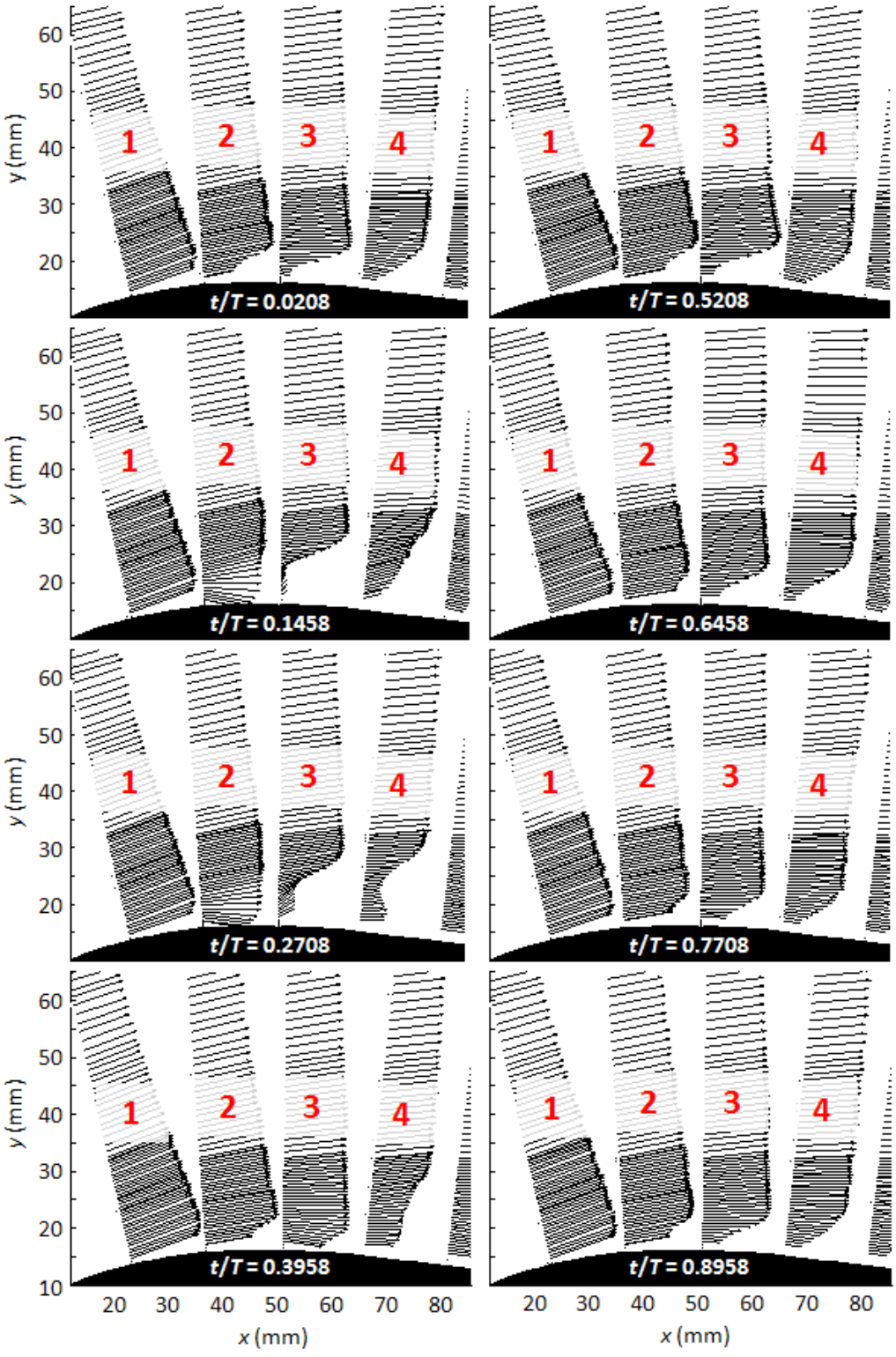

Figure 23: Ensemble-averaged streamwise velocity profiles for wakes + VGJs at 72%C_x (F_{red} = 0.41) at Re_c = 20,000. *Showing 8 of 24 measurement phases {1,4,7,10,13,16,19,22}.*

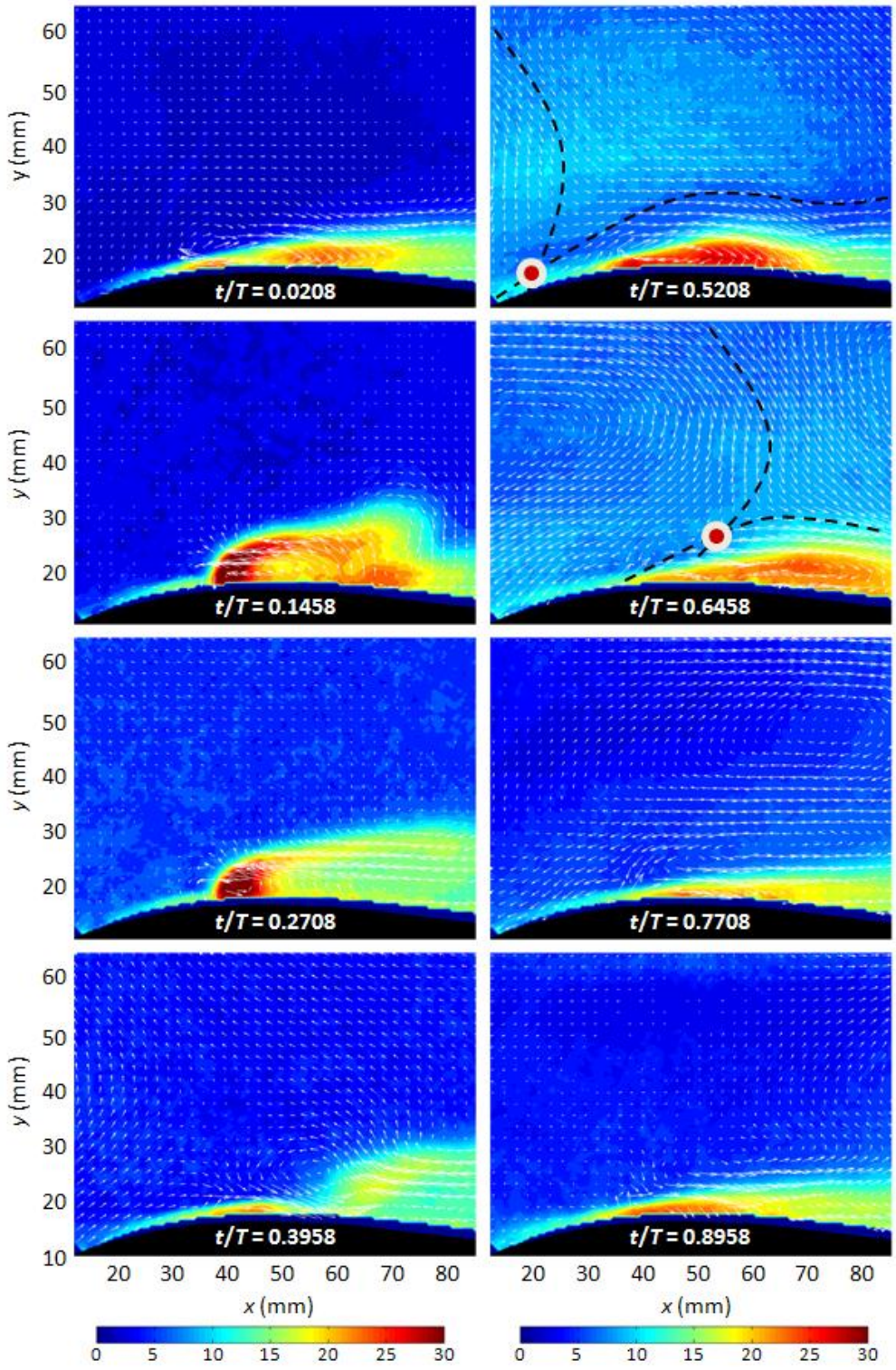

Figure 24: Contours of fluctuating velocity magnitude (U_{rms}/U_{in}) superposed with perturbation velocity vectors ($\Delta U_{mean}/U_{in}$), data for wakes + VGJs at 72%C_x (F_{red} = 0.41) at Re_c = 20,000. *Showing 8 of 24 measurement phases {phases 1,4,7,10,13,16,19,22}.*

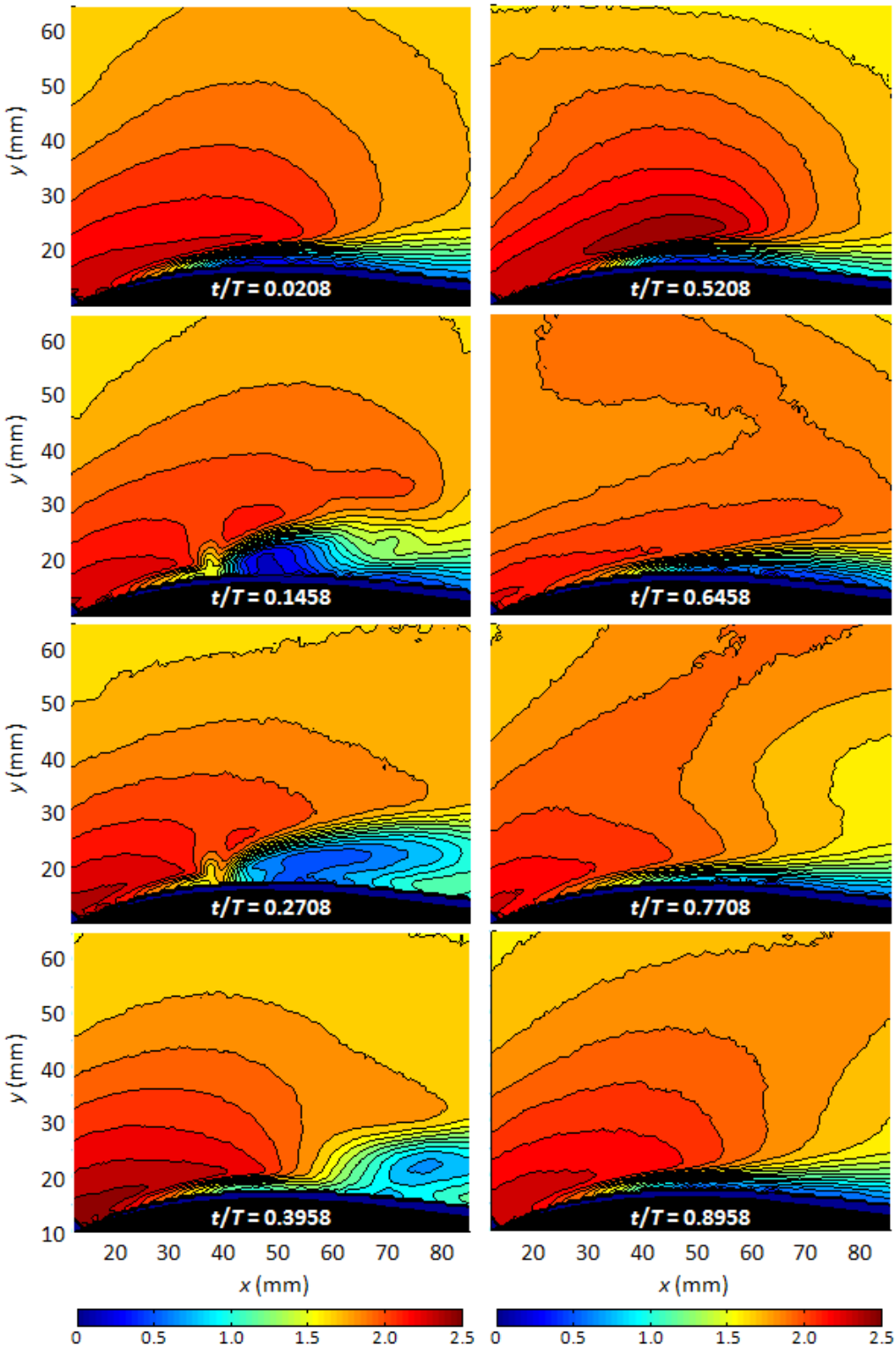

Figure 25: Contours of ensemble-averaged velocity magnitude (U_{mean}/U_{in}), data for wakes + VGJs at 72%C_x (F_{red} = 0.41) at Re_c = 20,000. *Showing 8 of 24 measurement phases.*

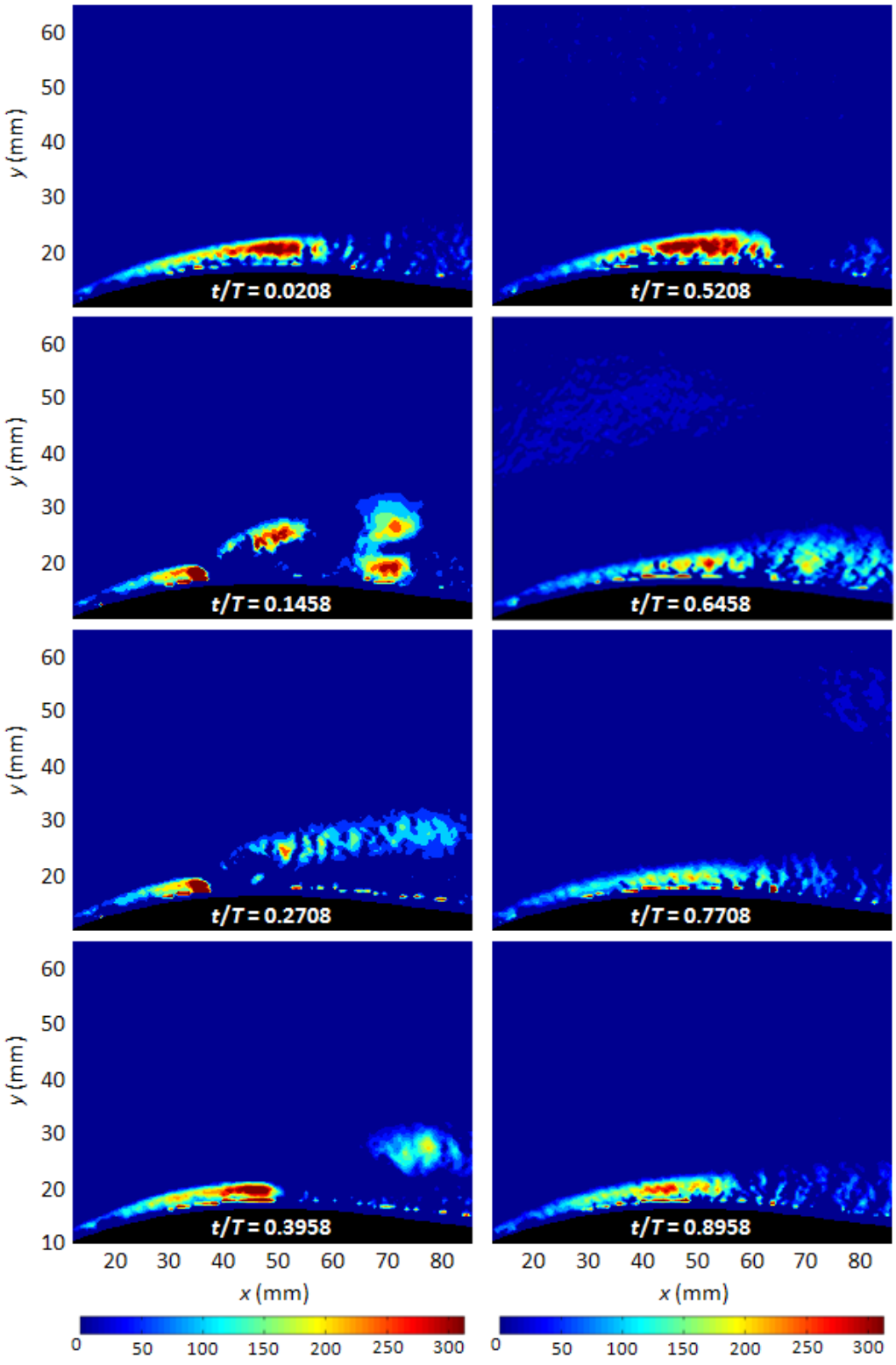

Figure 26: Contours of ensemble-averaged swirl strength (*Sw*), data for wakes-only (F_{red} = 0.41) at Re_c = 20,000. *Showing 8 of 24 measurement phases {phases 1,4,7,10,13,16,19,22}.*

II. L1A with Unsteady Wakes + VGJs, F_{red} = 0.41

The ensemble-averaged jet pulse signature shows that jet actuation occurs at t/T=0.01. The spanwise level for PIV data acquisition is 4d below the top of the nearest VGJ at the L1A midspan. Thus, jet fluid is not observed in this plane until t/T=0.06 (not shown), evidenced by elevated U_{rms}. At the onset of each pulse, the blowing ratio overshoot ($B_{max} \approx 3$) results in improved jet fluid penetration through the viscous layer (represented in Fig. 24 at t/T = 0.15). Moreover, the jet fluid furthest from the wall is bent in the downstream direction by the shear strain applied by the mean flow, and convects downstream through the domain until exiting between $0.23 < t/T < 0.27$. Contours of U_{mean}/U_{in} (Fig. 25) indicate fluid deceleration upstream of the jet as a result of the jet blockage, as well as a velocity deficit in the wake of the obstruction created by the VGJ. The main flow actually accelerates over the jet, resulting in the formation of a spanwise vortex of clockwise sense whose core is centered on and convects along with the initial jet fluid overshoot. Between $0.23 < t/T < 0.27$, the jet fluid is nearly steady, having been turned into the streamwise direction. After the jet terminates (by t/T = 0.31), the jet fluid convects off the surface between $0.31 < t/T < 0.4$. Flow accelerates over the clean surface with the boundary layer subdued by the VGJ disturbance. While not completely removed, and not attached, the boundary layer is thinned considerably between jet termination and the arrival of the wake disturbance. According to the single-element hot-film results obtained (see Appendix A), intermittency contours indicate that between $0.42 < t/T < 0.54$, the turbulent boundary layer is confined closest to the wall and the extent of laminar flow above the shear layer is greatest. The size of perturbation velocity vectors is maximal during this interval, with a peak value above the separated region of $\Delta U_{mean}/U_{in} \approx 1$. The maximum perturbation velocity magnitude just above the shear layer, associated with the Q1 vortex of the wake's negative jet is nearly twice that observed with wakes only. This is because of the combined benefit of fluid acceleration over VGJ-thinned

suction surface boundary layer as well as the positive streamwise perturbation of the wake. Together, these velocity perturbations enhance the streamwise momentum and suppress the separated shear layer better than either mechanism alone. Two-dimensional PIV data corroborates that the mean shear layer position is shifted downstream and confined closer to the suction surface, as evidenced by previously discussed hot-film results.

At t/T = 0.52 there is a slight increase in boundary layer thickness (Fig. 25) as Q1 has been interacting with separated fluid. Since the flow is not attached, and a separated shear layer prevails, wall-bound vorticity amplified by the elevated mean shear still causes the thin boundary layer to rollup into the Q3 vortex which can be seen at (x, y) = (52mm, 20mm). As previously shown in the wake-only case, as soon as Q2 begins to interact with the boundary layer, the velocity profile becomes less inflectional and a there is a reduction in peak unsteadiness by 7%U_{in} between 0.52 < t/T < 0.65 in the Q3 vortex core (27%U_{in} at t/T = 0.52; 21%U_{in} at t/T = 0.65). However, unlike the wake-only case, the formation of the near-wall Q4 vortex is not observed because it either does not exist or it is confined to close to the surface to be resolved in the current measurement configuration. Turbulence levels continue to decrease (0.65 < t/T < 0.90) as Q2 convects downstream, reaching levels between 12-20%U_{in}. Before the boundary layer can begin to recover, the subsequent jet pulse begins. Comparing contours of U_{mean}/U_{in} with those from the wake-only case, we can see that the freestream flow reaches higher speeds after the wake exits the domain. For instance, considering the wake-only case, at (x, y) = (90mm, 50mm), $U_{mean}/U_{in} \approx$ 1.6; whereas with wakes and jets, at the same location $U_{mean}/U_{in} \approx 1.9$, owning to the diminished separated region.

A significant difference in the character of the wake is observed when it impinges on the surface with a VGJ-thinned boundary layer. The flow is not completely attached under any test conditions at this spanwise location as indicated by the hot-film results. Therefore, there is a shear layer present, and because of this inflectional velocity profile, the boundary layer fluid is indeed

rolled up during its interaction with the wake's downstream-pointing perturbation as evidenced by a rise in boundary layer thickness which convects along with the perturbation. However, unlike the wake-only case, either the quadrupole structure does not form in this case, or the saddle point is so close to the wall that Q4 is not visible.

Assuming that the size of the boundary layer rollup vortices represented by Q4 are associated with the total pressure loss, the synergistic benefits achieved for optimal VGJ actuation at72%C_x can be summarized. The VGJs need to penetrate through the boundary layer in order to successfully entrain high momentum fluid and re-energize the boundary layer. The periodic wake disturbance facilitates jet penetration, which in turn results in a thinned boundary layer. Consequently, smaller rollup vortices are shed (presumably associated with the K-H instability) from within the boundary layer, especially during the wake-shear layer interaction, which ultimately results in reduction of observed aerodynamic losses.

CHAPTER FOUR: CONCLUSION

The suction side of a low pressure turbine blade is prone to laminar separation at low Reynolds numbers. Consequently, blade loading, total flow turning, and aerodynamic efficiency are diminished. The employment of flow control to mitigate these losses may expand flight envelopes, enable more aggressive designs, or by increasing available blade loading, reduce the blade count (component weight).

A new cascade facility was designed using the L1A blade which has a design Zweifel coefficient of 1.34 and a suction peak at 58% axial chord, making it an aft-loaded pressure distribution. Velocity and pressure data were acquired at Re_c = 20,000 with 3% incoming freestream turbulence. The L1A experiences a dramatic, non-reattaching separation at Reynolds numbers below 50,000. Design diffusion levels on the aft portion of the blade prove too aggressive for the laminar boundary layer at low Reynolds numbers. Unsteady wakes from an upstream vane row are simulated with a moving row of bars at a flow coefficient of 0.91. It was noted that the wake is preceded by accelerated incoming flow. The separation zone is modified substantially by the presence of unsteady wakes, producing a smaller separation zone and reducing the integrated wake total pressure loss by more than 75%. The wake disturbance accelerates transition in the separated shear layer but stops short of fully reattaching the flow. Rather, a new time-averaged equilibrium location is established for the separated shear layer, further downstream than without wakes.

With the application of flow control using a spanwise row of discrete vortex generator jets (VGJs) at 72%C_x, wake total pressure loss decreased 35% from the wake-only level and the

C_p distribution fully recovered its high Reynolds number performance. From detailed pressure data it is clear that the upstream VGJ disturbance (actuating at 58%C_x) dominates the dynamics of the separated shear layer, with the wake disturbance assuming a secondary role only. On the other hand, when actuating at 72%C_x, the jet disturbance assumes a secondary role, requiring more energy to penetrate through the separation zone. VGJ actuation at the downstream location inside the separated zone shows increased effectiveness by aligning the VGJ-induced calmed zone with the wake precursor between wake passing events. The addition of jets to the unsteady wake flowfield had the effect of moving the mean location of the shear layer downstream to a new quasi-stable equilibrium location. During the period between pulses, the shear layer did not migrate upstream to the wake only mean location or to the steady state location. This study sheds light on the essential physics that designers must understand to be able to successfully integrate VGJs into a new LPT design.

BIBLIOGRAPHY

[1] Mayle, R. E. (1991), "The Role of Laminar-Turbulent Transition in Gas Turbine engines," *ASME Journal of Turbomachinery , 113*, 509-537.

[2] Bohl, D. G., & Volino, R. J. (2006), "Experiments with Three-Dimensional Passive Flow control Devices on Low-Pressure Turbine Airfoils," *ASME Journal of Turbomachinery , 128*, 251-260.

[3] Volino, R. J. (2003). "Passive Flow Control on Low-Pressure Turbine Airfoils," *ASME Journal of Turbomachinery , 125*, 752-764.

[4] Huang, J., Corke, T., & Thomas, F. (2006), "Plasma Actuators for Separation Control on Low Pressure Turbine Blades," *AIAA Journal , 44* (1), 51-57.

[5] Volino, R. J. (2003), "Separation Control on Low-Pressure Turbine Airfoils Using Synthetic Vortex Generator Jets," *ASME Journal of Turbomachinery , 125*, 765-777.

[6] Zheng, X., Zhou, S., Lu, Y., Hou, A., Li, Q., (2008), "Flow Control of Annular Compressor Cascade by Synthetic Jets," *ASME Journal of Turbomachinery,130*.

[7] Johari, H., & Rixon, G. S. (2003), "Effects of Pulsing on a Vortex Generator Jet," *AIAA Journal , 41* (12).

[8] Reimann, D., Bloxham, M., Pluim, J., & Bons, J. P. (2007), "Comparison of Spanwise Wake and Discrete Jet Disturbances on a Separating Low-Pressure Turbine Blade," *AIAA 45th Aerospace Sciences Meeting*. Reno, NV.

[9] Bons, J. P., Pluim, J., Gompertz, K., Bloxham, M., & Clark, J.P., (2008), "The Application of Flow Control to an Aft-Loaded Low Pressure Turbine Cascade with Unsteady Wakes," *ASME Turbo Expo 2008: Power for Land, Sea and Air*. Berlin, June, 2008. Paper #GT2008-50864.

[10] Bons, J. P., Sondergaard, R., & Rivir, R. B. (2002), "The Fluid Dynamics of LPT Blade Separation Control Using Pulsed Jets," *ASME Journal of Turbomachinery , 124*, 77-85.

[11] Sondergaard, R., Bons, J. P., & Rivir, R. B. (2002), "Control of Low-Pressure Turbine Separation Using Vortex Generator Jets," *AIAA Journal of Propulsion and Power , 18* (4), 889-895.

[12] McQuilling, M., & Jacob, J. (2004), "Effect of chord Location on Separation Control with Vortex Generator Jets on Low Pressure Turbine Blades," *2nd AIAA Flow Control Conference*. Portland, OR.

[13] Olson, D. H., Reimann, D., Bloxham, M., & Bons, J. P. (2005), "The Effect of Elevated Freestream Turbulence on Separation Control with Vortex-Generating Jets," *AIAA 43rd Aerospace Sciences Meeting*. Reno, NV.

[14] Bloxham, M., Reimann, D., Crapo, K., Pluim, J., & Bons, J. P. (2007), "Synchronizing Separation Flow Control with Unsteady Wakes in a Low-Pressure Turbine Cascade," *IGTI*. Montreal.

[15] Gross, A., & Fasel, H. F. (2004), "Active Control of Separation for Low-Pressure Turbine Blades," *AIAA 2nd Flow Control Conference*. Portland, OR.

[16] Sondergaard, R., Bons, J. P., & Rivir, R. B. (2002), "Reducing Low-Pressure Turbine Stage Blade Count Using Vortex Generator Jet Separation Control," *IGTI Conference*. Amsterdam, The Netherlands.

[17] Bons, J. P., Hansen, L. C., Clark, J. P., Koch, P. J., & Sondergaard, R. (2005), "Designing Low-Pressure Turbine Blades with Integrated Flow Control," *IGTI Conference*. Reno, NV.

[18] Reimann, D., Bloxham, M., Crapo, K. L., Pluim, J. D., & Bons, J. P. (2006), "Influence of Vortex Generator Jet-Induced Transition on Separating Low Pressure turbine Boundary Layers," *3rd AIAA Flow Control Conference*. San Francisco, CA.

[19] Praisner, T. J., Grover, E. A., Rice, M. J., & Clark, J. P. (2004), "Predicting Transition in Turbomachinery, Part 2-Model Validation and Benchmarking"

[20] McQuilling, M., Wolff, M., Fonov, S., Crafton, J., Sondergaard, R. (2008), "An Experimental Investigation of Suction Surface Flow Features on a High-Lift LPT," *AIAA 46th Aerospace Sciences Meeting 2008*. Reno, NV.

[21] Praisner, T. J., & Clark, J. P. (2007), "Predicting Transition in Turbomachinery, Part 1-A Review and New Model Development," *ASME Journal of Turbomachinery , 129*, 1-13.

[22] Clark, J. P., & Grover, E. A. (2007), "Assessing Convergence in Predictions of Periodic-Unsteady Flowfields," *ASME Journal of turbomachinery , 129* (4), 740-749.

[23] Dorney, D. J., & Davis, R. L. (1992), "Navier-Stokes Analysis of Turbine Blade HEat Transfer and Performance," *ASME Journal of Turbomachinery , 114*, 795-806.

[24] Volino, R. J. (2008), "Separated Flow Measurements on a Highly Loaded Low-Pressure Turbine Airfoil," *ASME Turbo Expo 2008: Power for Land, Sea and Air*. Berlin.

[25] Ozturk, B., & Schobeiri, M. T. (2006), "Effect of Turbulence Intensity and Periodic Unsteady Wake Flow Condition on Boundary Layer Development, Separation, and Re-attachment over the Separation Bubble along the Suction Surface of a Low-Pressure Turbine Blade," *ASME Turbo Expo 2006: Power for Land, Sea, and Air*.

[26] Uzol, O., Zhang, X. F., Cranstone, A., & Hodson, H. (2007), "Investigation of Unsteady Wake-Separated Boundary Layer Interaction Using Particle-Image-Velocimetry," *ASME Turbo Expo 2007: Power for Land, Sea, and Air*. Montreal.

[27] Wolff, S., Brunner, S., & Fottner, L. (2000), "The use of Hot-Wire Anemometry to Investigate Unsteady Wake-Induced Boundary-Layer Development on a High Lift LPT Cascade," *ASME Turbo Expo 2000: Power for Land, Sea, and Air*.

[28] Kaszeta, R. W., Simon, T. W., & Ashpis, D. E. (2001), "Experimental Investigation of Transition to Turbulence as Affected by Passing Wakes," *ASME Turbo Expo 2001: Power for Land, Sea, and Air*.

[29] Steiger, R., Hollis, D., & Hodson, H. (2003), "Unsteady Surface Pressures Due to Wake Induced Transition in a Laminar Separation Bubble on a LP Turbine Cascade," *ASME Turbo Expo 2003: Power for Land, Sea, and Air*.

[30] Mahallati, A., & Sjolander, S. (2007), "Aerodynamics of a Low-Pressure Turbine Airfoil at Low-Reynolds Numbers, Part 2: Blade-Wake Interaction," *ASME Turbo Expo 2007: Power for Land, Sea, and Air*.

[31] Schulte, V., & Hodson, H. P. (1998), "Unsteady Wake-Induced Boundary Layer Transition in High Lift LP Turbines," *ASME Journal of Turbomachinery , 120*, 28-35.

[32] Lou, W., & Hourmouziadis, J. (2000), "Separation Bubbles Under Steady and Periodic-Unsteady Main Flow Conditions," *ASME Turbo Expo 2000: Power for Land, Sea, and Air.*

[33] Cattenei, A., Zuinino, P., Schroder, T., Stoffel, B., & Matyschok, B. (2006), "Detailed Analysis of Experimental Investigations on boundary Layer Transition in Wake Disturbed Flow," *IGTI Conference*. Barcelona.

[34] Steiger, R. D., & Hodson, H. P. (2004), "The Transition Mechanism of Highly Loaded Low-Pressure Turbines," *ASME Journal of Turbomachinery , 126*, 536-543.

[35] Meyer, R. X. (1958, October), "The Effect of Wakes on the Transient Pressure and Velocity Distribution in Turbomachines," *Transactions of the ASME* , 1544-1552.

[36] McAuliffe, B. R., & Yaras, M. I. (2007), "Transition Mechanisms in Separation Bubbles Under Low and Elevated Freestream Turbulence," *ASME Turbo Expo 2007: Power for Land, Sea and Air.* Montreal.

[37] McAuliffe, B. R., & Yaras, M. I. (2006), "Numerical Study of Instability Mechanisms Leading to Transition in Separation Bubbles," *ASME Turbo Expo 2006: Power for Land, Sea and Air.* Barcelona.

[38] Crawford, M. E., & Kays, W. M., "STAN5 -- A Program for Numerical Computation of Two-Dimensional Internal and External Boundary Layer Flows," *Contractor Report*, NASA.

[39] Eldredge, R. G., & Bons, J. P. (2004), "Active Control of a Separating Boundary Layer with Steady Vortex Generating Jets--Detailed Flow Measurements," *42nd AIAA Aerospace Sciences Meeting.* Reno, NV.

[40] Bons, J. P., Bloxham, M., & Reimann, D. (2006), "Separated Flow Transition on an LP Turbine Blade with Pulsed Flow Control," *IGTI Conference*. Barcelona.

[41] LaVision. (2004). *Davis Flowmaster*. (A.-V.-R. 19, Ed.) Gottingen: LaVision GmbH.

[42] Zhou, J., Adrian, R. J., & Balachandar, S. (1996), "Autogeneration of Near Wall Vortical Structures in Channel Flow," *Physics of Fluids , 8*, 288-290.

[43] Zhou, J., Adrian, R. J., Balachandar, S., & Kendall, T. M. (1999), "Mechanisms for Generating Coherent Packets of Hairpin vortices in Channel Flow," *Journal of Fluid Mechanics , 387*, 353-359.

[44] Adrian, R. J., Christensen, K. T., & Liu, Z. -C. (2000), "Analysis and interpretation of instantaneous turbulent velocity fields," *Experiments in Fluids , 29*, 275-290.

[45] Coleman, H. W., & Steele, W. G. (1999). *Experimentation and Uncertainty Analysis for Engineers* (2 ed.). Canada: Wiley-Interscience.

APPENDIX A: Intermittency Data

Figures 27 and 28show contours of intermittency for all 24 measurement phases of the wake-only and wake + VGJ (actuating at 72%C_x) for F_{red} = 0.41. The data are presented with the wall normal distance from the suction side along the ordinate and axial chord location indicated on the abscissa.

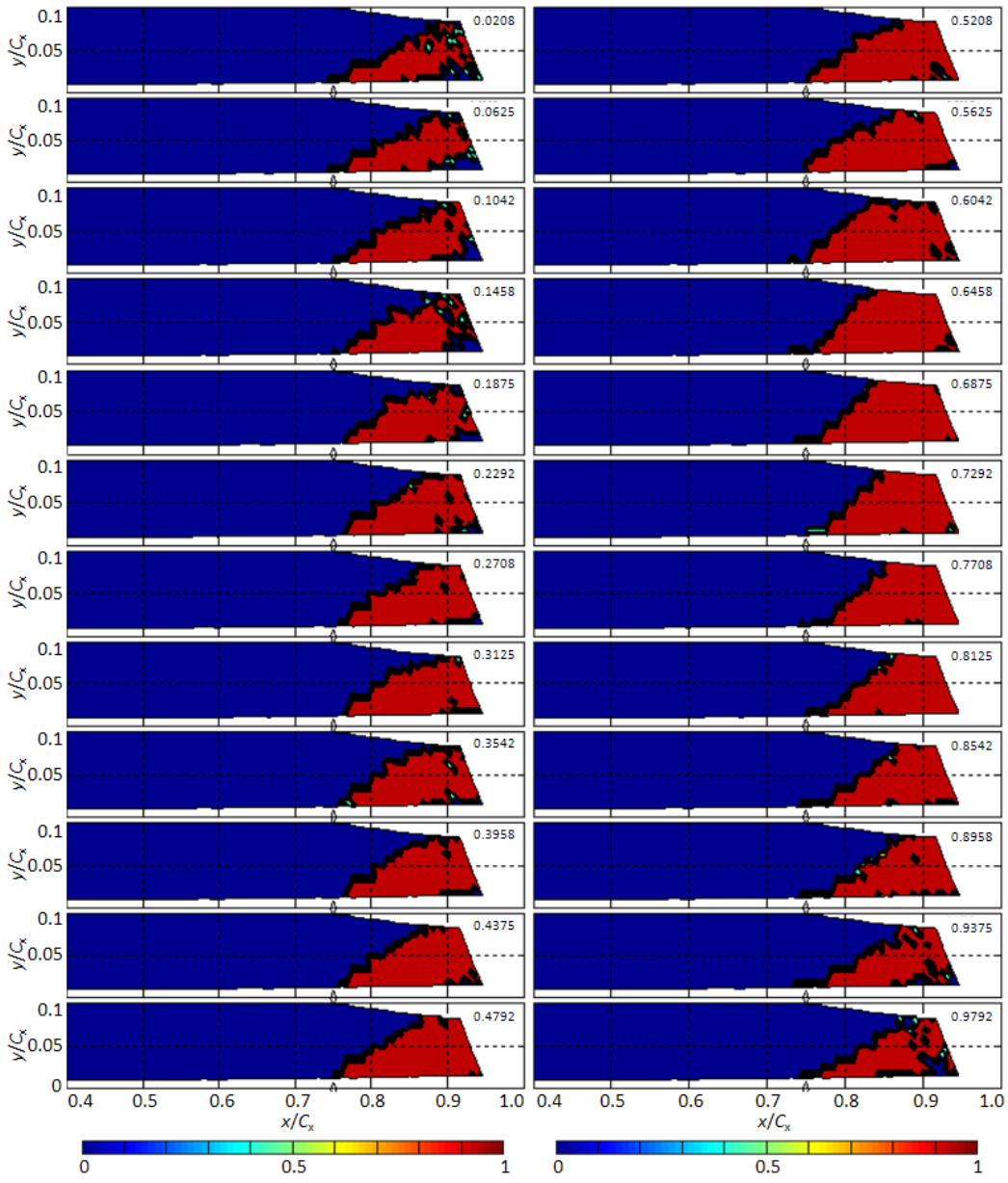

Figure 27: Contours of intermittency for wakes-only (F_{red} = 0.41), Re_c = 20,000. *Showing all 24 measurement phases.*

Comparing the two figures, it is clear that the extent of laminar flow over the suction surface is greatest, and the turbulent boundary layer is confined closest to the surface for wakes + jets between $0.42 < t/T < 0.54$.

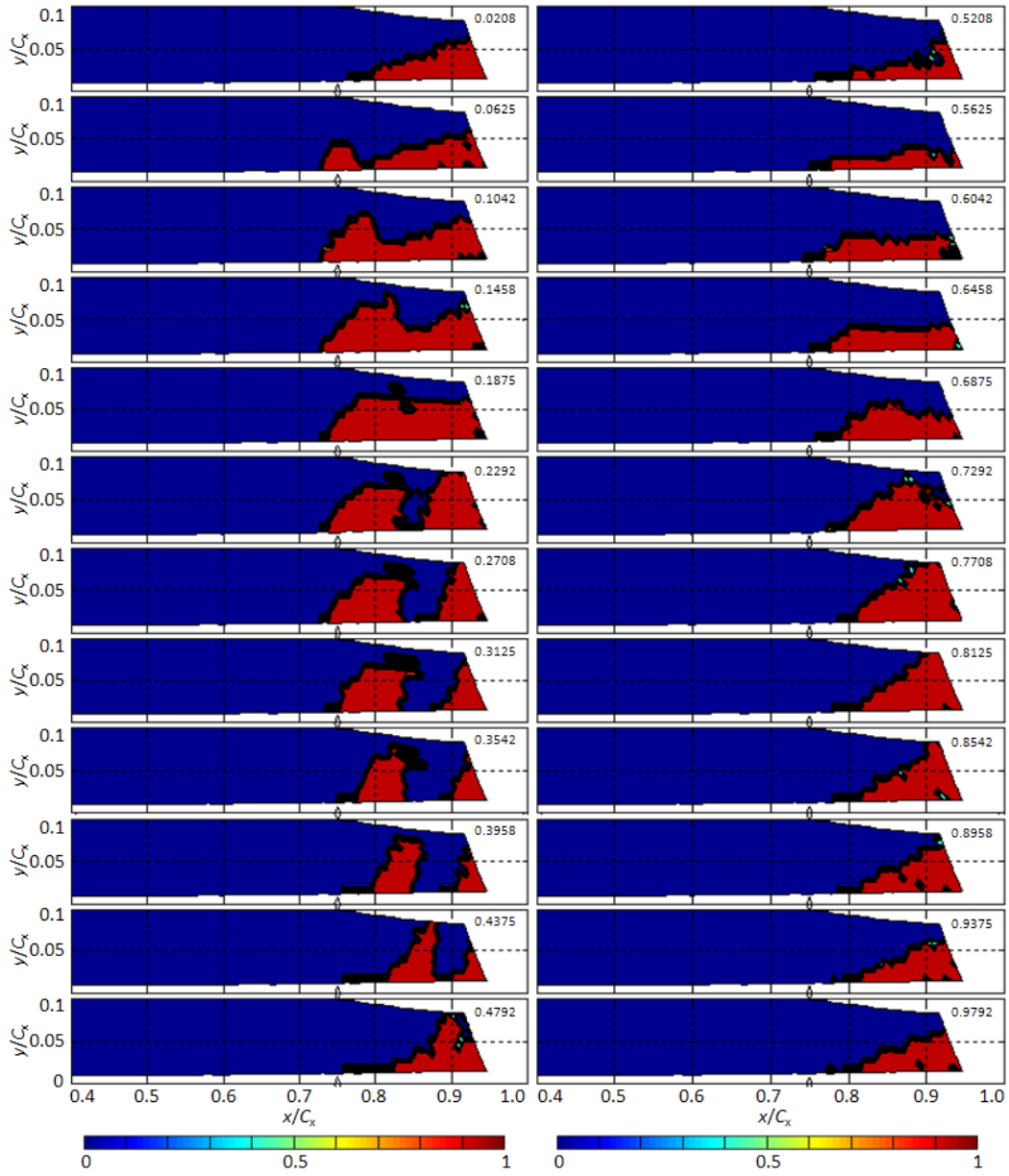

Figure 28: Contours of intermittency for wakes + VGJs at 72%C_x (F_{red} = 0.41), Re_c = 20,000. *Showing all 24 measurement phases.*

APPENDIX B: Instantaneous PIV images

Figure 29 is a collage of PIV snapshots showing streamlines for six representative phases during the wake-passing period of the wake-only case (no VGJs). For each image shown, the streamlines are computed for a single image pair. The interval between images ($\Delta t/T$ = 100μs) is short enough to resolve the existence of large-scale vortical motion within the flow field, indicated by streamlines that spiral into vortices. Phases 3, 4, and 5 precede the arrival of the wake in the measurement domain. The images in the left column of Fig. 29 provide evidence of vortex shedding from within the separated boundary layer. Phases 10, 12, and 17 are during the wake's interaction with the separated boundary layer. Evidence of vortex shedding is difficult to identify by observing the streamlines from image pairs acquired during phases 10 and 17, as shown by the typical images in Fig. 29. The character of images acquired during phases 12 – 15 is represented in Fig. 29 by the snapshot for phase 12. In this image, there is evidence of a vortex which is presumably the shear layer rollup (Q4 in the ensemble-averaged data).

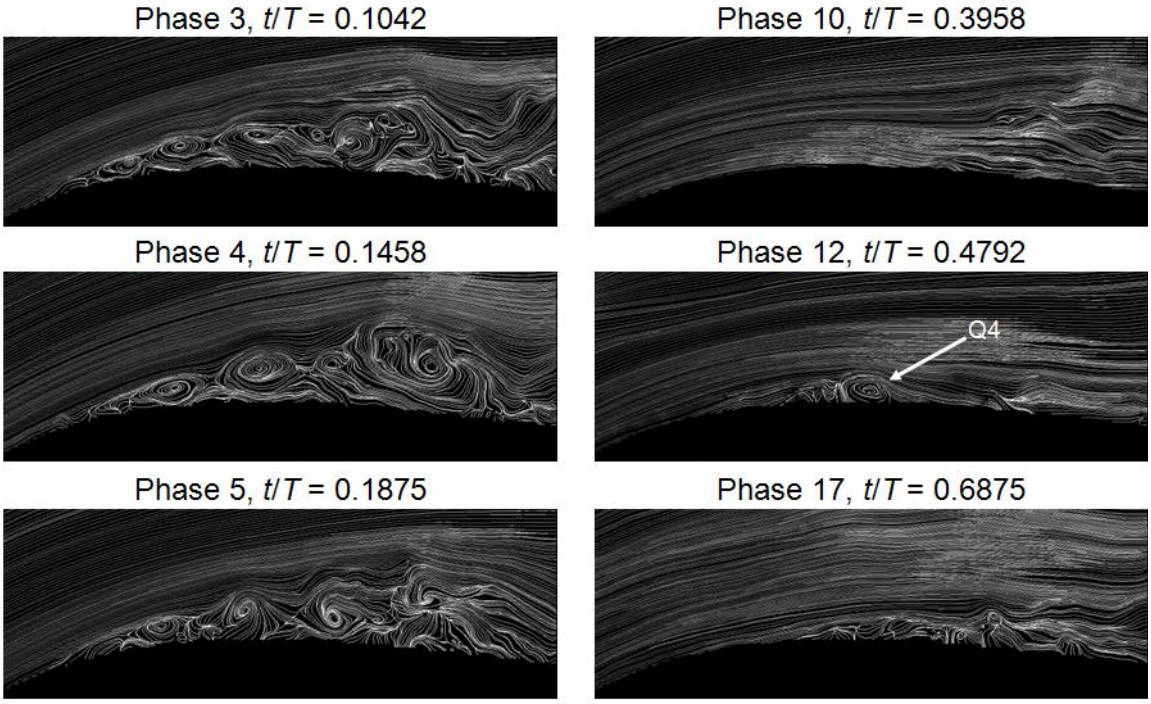

Figure 29: Collage of representative snapshots throughout the wake-passing period showing streamlines for wake-only case (F_{red} = 0.41), Re_c = 20,000.